



# Core Protein-Directed Antivirals and Importin $\beta$ Can Synergistically Disrupt Hepatitis B Virus Capsids

Christine Kim,<sup>a</sup> Lauren F. Barnes,<sup>b</sup> Christopher J. Schlicksup,<sup>a</sup> Angela J. Patterson,<sup>c</sup> Brian Bothner,<sup>c</sup> Martin F. Jarrold,<sup>b</sup> Che-Yen Joseph Wang,<sup>d</sup> Adam Zlotnick<sup>a</sup>

<sup>a</sup>Department of Molecular & Cellular Biochemistry, Indiana University, Bloomington, Indiana, USA

<sup>b</sup>Department of Chemistry, Indiana University, Bloomington, Indiana, USA

<sup>c</sup>Department of Chemistry & Biochemistry, Montana State University, Bozeman, Montana, USA

<sup>d</sup>Department of Microbiology & Immunology, Pennsylvania State University College of Medicine, Hershey, Pennsylvania, USA

**ABSTRACT** Viral structural proteins can have multiple activities. Antivirals that target structural proteins have potential to exhibit multiple antiviral mechanisms. Hepatitis B virus (HBV) core protein (Cp) is involved in most stages of the viral life cycle; it assembles into capsids, packages viral RNA, is a metabolic compartment for reverse transcription, interacts with nuclear trafficking machinery, and disassembles to release the viral genome into the nucleus. During nuclear localization, HBV capsids bind to host importins (e.g., Imp $\beta$ ) via Cp's C-terminal domain (CTD); the CTD is localized to the interior of the capsid and is transiently exposed on the exterior. We used HAP12 as a representative Cp allosteric modulator (CpAM), a class of antivirals that inappropriately stimulates and misdirects HBV assembly and deforms capsids. CpAM impact on other aspects of the HBV life cycle is poorly understood. We investigate how HAP12 influences the interactions between empty or RNA-filled capsids with Imp $\beta$  and trypsin *in vitro*. We show that HAP12 can modulate CTD accessibility and capsid stability, depending on the saturation of HAP12-binding sites. We demonstrate that Imp $\beta$  synergistically contributes to capsid disruption at high levels of HAP12 saturation, using electron microscopy to visualize the disruption and rearrangement of Cp dimers into aberrant complexes. However, RNA-filled capsids resist the destabilizing effects of HAP12 and Imp $\beta$ . In summary, we show host protein-induced catalysis of capsid disruption, an unexpected additional mechanism of action for CpAMs. Potentially, untimely capsid disassembly can hamper the HBV life cycle and also cause the virus to become vulnerable to host innate immune responses.

**IMPORTANCE** The HBV core, an icosahedral complex of 120 copies of the homodimeric core (capsid) protein with or without packaged nucleic acid, is transported to the host nucleus by its interaction with host importin proteins. Importin-core interaction requires the core protein C-terminal domain, which is inside the capsid, to “flip” to the capsid exterior. Core protein-directed drugs that affect capsid assembly and stability have been developed recently. We show that these molecules can, synergistically with importins, disrupt capsids. This mechanism of action, synergism with host protein, has the potential to disrupt the virus life cycle and activate the innate immune system.

**KEYWORDS** HBV, antiviral, assembly, capsid, karyopherin

Chronic hepatitis B virus (HBV) infection is endemic and, though not a regular discussion in the daily news, a global health crisis (1). Chronic HBV afflicts approximately 300 million people and can lead to cirrhosis, hepatocellular carcinoma, and liver failure; it contributes to about 880,000 deaths annually (2). Although there is an effective vaccine available, it does not help those who are chronically infected. Current

**Editor** J.-H. James Ou, University of Southern California

**Copyright** © 2022 American Society for Microbiology. All Rights Reserved.

Address correspondence to Adam Zlotnick, azlotnic@indiana.edu.

We declare a conflict of interest. A.Z. is a founder and has an interest in biotech companies that develop assembly-directed antivirals.

**Received** 13 August 2021

**Accepted** 19 October 2021

**Accepted manuscript posted online** 27 October 2021

**Published** 26 January 2022

therapeutics (mainly directed against the viral DNA polymerase) are rarely curative, so there is a great need to develop new and better antivirals.

An attractive drug target for new HBV therapeutics is the core protein (Cp) (3). The Cp plays roles in most stages of the viral life cycle: assembling on and encapsidating viral RNA and polymerase, acting as a metabolic compartment for reverse transcription to DNA, and regulating capsid transport to the nucleus to maintain infection or to the endoplasmic reticulum (ER) to be secreted (4–6). Most capsids are composed of 120 homodimers arranged with  $T = 4$  icosahedral symmetry. A small fraction of capsids have 90 dimers with  $T = 3$  symmetry. Dimers associate through weak hydrophobic contacts at the interdimer interfaces (7). Cp has an assembly domain (residues 1 to 149) and a nucleic acid-binding C-terminal domain (CTD; residues 150 to 183). During viral replication, approximately 90% of capsids are without a viral genome (8). In  $T = 4$  capsids, Cp is found as quasi-equivalent A, B, C, and D monomers, which form AB and CD dimers. The interface between two dimers forms a small hydrophobic pocket, which can be probed with small molecules (4, 9).

Core protein allosteric modulators (CpAMs) are small molecules that can probe HBV capsids by binding to interdimer contacts (10). Heteroaryldihydropyrimidines (HAPs) are a class of CpAMs that have been extensively studied for their ability to accelerate and misdirect capsid assembly (11–13). When bound at Cp-Cp contact sites in the HAP pocket, HAPs increase the association energies of dimer-dimer contacts. Cp assembled in the presence of HAPs can produce aberrant structures with various morphologies, depending on the CpAM chemotype (13–15). HAPs can also cause capsid deformation by disturbing the capsid's icosahedral geometry. When incubated with the molecule HAP-6-carboxytetramethylrhodamine (TAMRA), capsid quasi-6-fold vertices became flattened, a defect that can propagate to yield highly irregular particles (15). Thus, not only do these antivirals impair capsid assembly, they can also target morphologically "normal" capsids, even "melting" virions to prevent infection (16, 17). Although we understand how HAPs influence the capsid's structure, it is still poorly understood how HAP-induced deformation impacts HBV biology in an infected cell.

Much of HBV Cp biology is a function of the CTDs. The CTDs are intrinsically disordered and positively charged (16 arginines out of 34 residues). In the context of an icosahedral capsid, CTDs are clustered around quasi-6-fold and 5-fold vertices (18). CTDs play important roles in RNA packaging and regulating reverse transcription (19–21). Though they are ostensibly on the inside of the capsid, they can transiently flip out to the capsid exterior to expose nuclear localization signals (22–26). The organization and mobility of CTDs are influenced by phosphorylation and nucleic acid content (27–30). In the nucleic acid-filled particles, CTDs electrostatically interact with the negatively charged nucleic acid and stay primarily internalized (18). During infection, capsids, containing relaxed circular DNA (rcDNA), can localize to the nucleus via interaction with host importins  $\alpha$  (Imp $\alpha$ ) and  $\beta$  (Imp $\beta$ ) (31). Once the capsid is imported into the nuclear pore complex, the capsid protein interacts with nucleoporin 153, disassembles, and releases its genome (32, 33). Previously, it was shown that both Imp $\alpha$  and Imp $\beta$  were required for nuclear trafficking (33–35). However, Imp $\beta$  can directly bind to the empty capsids or dimers without the presence of Imp $\alpha$  and can be internalized (26).

Here, we examine how CpAMs affect CTD mobility. How these antivirals impact other aspects of the life cycle is still unclear. For these studies, we use the CpAM HAP12, which has strong Cp-binding activity *in vitro* and efficacy *in vivo* (13). HAP12 is structurally very similar to GLS4 (12). In this study, we investigated how HAP12 binding affects the CTD's ability to interact with Imp $\beta$ . We found that the CTD's mobility increased with high HAP12 stoichiometry, causing more CTD-Imp $\beta$  binding. Surprisingly, excess HAPs led to capsid disruption in empty particles. However, despite excess HAPs, capsids with internal RNA did not experience greater Imp $\beta$  binding and were able to maintain their structural integrity. In this work, we show how two exogenous molecules work synergistically to destabilize HBV capsids. Our study also investigates how a second antiviral mechanism of action, capsid dissociation, is modulated by CpAMs and host proteins.

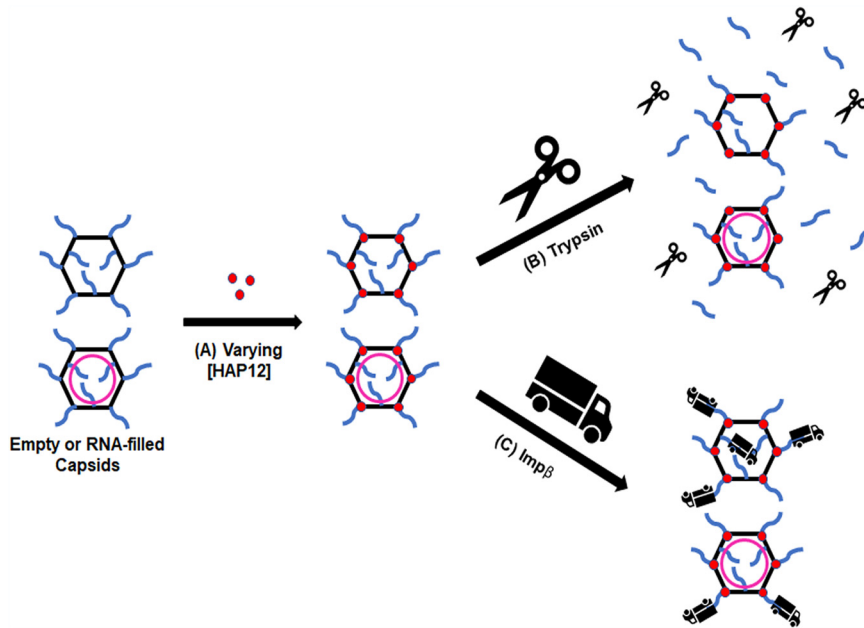


**FIG 1** Capsid proteolysis and Imp $\beta$  binding experimental schematic. (A) Empty and RNA-filled capsids were initially treated with various concentrations of the CpAM HAP12 and then interrogated by proteolysis or Imp $\beta$  binding. Trypsin is represented by scissors, and Imp $\beta$  is represented by trucks. HAP12 treatment was characterized in terms of “saturation”: at saturating HAP12 concentrations, there is one active HAP12 molecule for every HAP pocket. (B) HAP12-treated empty, pgRNA-filled, and *E. coli* RNA-filled capsids were digested with trypsin, and reactions were quenched before proteolyzed products were resolved using SDS-PAGE and LC-MS. (C) HAP12-treated empty and *E. coli* RNA-filled capsids were mixed with Imp $\beta$  and dialyzed into a low-NaCl-concentration buffer to allow binding. Imp $\beta$ -bound capsids were analyzed using SEC, SDS-PAGE, TEM, and CDMS.

## RESULTS

**Capsid proteolysis and Imp $\beta$  binding experimental schematic.** HAPs, like many CpAMs, cause capsid deformation and even disruption on a global level (14, 15). Because Cp dimers appear to be relatively rigid and CpAMs bind at the interface between dimers, deformation is likely to be manifested in the dimer-dimer geometry and at vertices. CTDs are clustered around 5-fold and quasi-6-fold vertices; therefore, we anticipated that HAPs would change the external exposure of CTDs.

To test our prediction that CpAMs modulate CTD exposure, we determined the effect of the CpAM HAP12 on CTD susceptibility to proteolysis and the CTD’s ability to bind Imp $\beta$  (Fig. 1A and B). Imp $\beta$  binds a basic peptide of ca. 40 amino acids (36), much longer than a typical nuclear localization sequence (NLS); therefore, Imp $\beta$  is a sensitive tool for probing CTD exposure. The impact of CpAMs on CTD exposure has not previously been tested. Complicating this test, the effect of a HAP on assembly is highly dose dependent. At low ratios of HAP to Cp, morphologically normal capsids form, whereas when HAP is superstoichiometric—that is, there is more than one active HAP per subunit—abnormal polymers assemble (13, 14). For this reason, we wanted to examine how different ratios of CpAM modulated CTD exposure.

**High concentrations of the CpAM HAP12 change the CTD proteolysis pattern.** Low HAP12/dimer ratios stabilize empty capsids and were predicted to decrease CTD proteolysis. Conversely, supersaturating ratios of HAP12, which cause capsid deformation even with intact capsids, were predicted to make empty capsids more vulnerable to proteolysis. To test this, empty capsids were treated with HAP12 and proteolyzed with trypsin, and the digested products were analyzed by SDS-PAGE and liquid chromatography-mass spectrometry (LC-MS). For these experiments, 7  $\mu$ M Cp183 dimer was used. The HAP12 ratio was calculated by accounting for HAP12’s racemic mixture, half of which is inactive, and by taking into account that each dimer forms two HAP-binding sites. Therefore, we

**TABLE 1** Curve fitting of CTD proteolysis data as a 2-first-order decay<sup>a</sup>

| Sample                                            | Population 1<br>mole fraction | Population 1<br>$t_{1/2}$ (min) | Population 2<br>mole fraction | Population 2<br>$t_{1/2}$ (min) | RMSD   |
|---------------------------------------------------|-------------------------------|---------------------------------|-------------------------------|---------------------------------|--------|
| Empty capsid                                      | 0.37                          | 0.42                            | 0.43                          | 6.58                            | 0.0065 |
| Empty + subsaturating HAP12                       | 0.35                          | 0.35                            | 0.50                          | 9.37                            | 0.0105 |
| Empty + saturating HAP12                          | 0.28                          | 0.40                            | 0.60                          | 5.51                            | 0.0132 |
| Empty + supersaturating HAP12                     | 0.74                          | 0.47                            | 0.25                          | 2.40                            | 0.0033 |
| pgRNA-filled capsid                               | 0.21                          | 0.36                            | 0.65                          | 9.83                            | 0.0101 |
| pgRNA capsid + supersaturating HAP12              | 0.24                          | 0.29                            | 0.72                          | 7.73                            | 0.0099 |
| <i>E. coli</i> RNA-filled capsid                  | 0.24                          | 0.28                            | 0.12                          | 13.97                           | 0.0041 |
| <i>E. coli</i> RNA capsid + supersaturating HAP12 | 0.20                          | 0.05                            | 0.53                          | 15.51                           | 0.0068 |

<sup>a</sup>Cp183 cleavage is in terms of populations cleaved rapidly (population 1), cleaved slowly (population 2), and uncleaved ( $1.0 - \text{population 1} - \text{population 2}$ ). The mole fractions of these three populations sum to 1.0.  $t_{1/2}$ , half-life; RMSD, root mean square difference.

used 14  $\mu\text{M}$  HAP12 as a subsaturating concentration, 28  $\mu\text{M}$  as saturating, and 56  $\mu\text{M}$  as supersaturating. These concentrations are well above the dissociation constant of HAP12 for capsid, so it is assumed that all active HAP12 is bound (13). These concentrations corresponded to 1 active HAP12 molecule per dimer, 2 active HAP12 molecules per dimer, and 4 active HAP12 molecules per dimer, respectively.

Because different HAP12 regimens have different effects on capsid stability, we examined how they affected the kinetics of CTD exposure. The trypsin concentration for these experiments was chosen to avoid the much slower cleavage of the assembly domain (37). The loss of the parent, Cp183, was expected to yield first-order kinetics. Cp183 and cleavage products were visualized by SDS-PAGE and normalized to the total optical density of a given lane. For all nontreated and HAP12-treated data sets, a single exponential fit showed systematic differences in the rates of proteolysis. Data were well fit by two first-order decays:  $[\text{Cp183}] = B_1 e^{-x \cdot [1/k1]} + B_2 e^{-x \cdot [1/k2]} + (1 - B_1 - B_2)$ . Coefficients  $B_1$  and  $B_2$  are the fractions of Cp183 in each of two populations of CTDs (Table 1), with  $k1$  and  $k2$  as the respective rate constants. A population of uncleaved CTD is explicit in the final term of this equation. With from no HAP12 to saturating HAP12, the fast-cleaving CTDs of empty capsids accounted for  $33\% \pm 5\%$  of the Cp183, with a half-life of  $0.4 \pm 0.03$  min. For the slow-cleaving population, the proteolysis accounted for  $51\% \pm 8\%$ , with a half-life of  $7 \pm 2$  min. At superstoichiometric HAP12, 74% of CTDs were rapidly cleaved, with a half-life of 0.47 min; the remaining 25% had a half-life of 2.40 min.

The cleavage kinetics for drug-free to saturated-HAP12 data sets were very similar. It is not until there was supersaturating HAP12 that we observed significant changes. Our data showed that HAP12 does not change CTD exposure in empty capsids until HAP12 reaches superstoichiometric concentrations, at which it can induce capsid deformation that would expose more CTDs. Another issue to consider is whether the  $T = 4$  symmetry modulates cleavage kinetics; i.e., rates correspond to the A, B, C, and D subunits. The 33% average coefficient for the fast cleavage rate is far enough from the value of 25% predicted by quasi-equivalence that quasi-equivalence seems an unlikely explanation. We suggest that cleavage rates may be affected by progressive charge changes within the capsid during proteolysis, as well as capsid heterogeneity along with quasi-equivalence.

The pattern of CTD cleavage is also affected by capsid content. For HAP12-free empty capsids, proteolysis with trypsin yielded three doublets of cleaved Cp183 and a faint seventh band by SDS-PAGE (Fig. 2A). For empty capsids treated with supersaturating HAP12, all Cp was proteolyzed to the lowest-molecular-weight band (Fig. 2A). Reaction mixtures were further analyzed by LC-MS to identify SDS-PAGE bands. The highest-molecular-weight band corresponded to Cp183, and the lowest-molecular-weight band corresponded to the 150 N-terminal residues of Cp (Fig. 2A). Other LC-MS data indicated cleavage after residues 175, 157, 152, and 151 (Fig. 2A). These findings are consistent with those of previous CTD proteolysis studies (28).

We anticipated that pregenomic RNA (pgRNA)-filled capsids would be more resistant to proteolysis than empty capsids since electrostatic interactions between the RNA

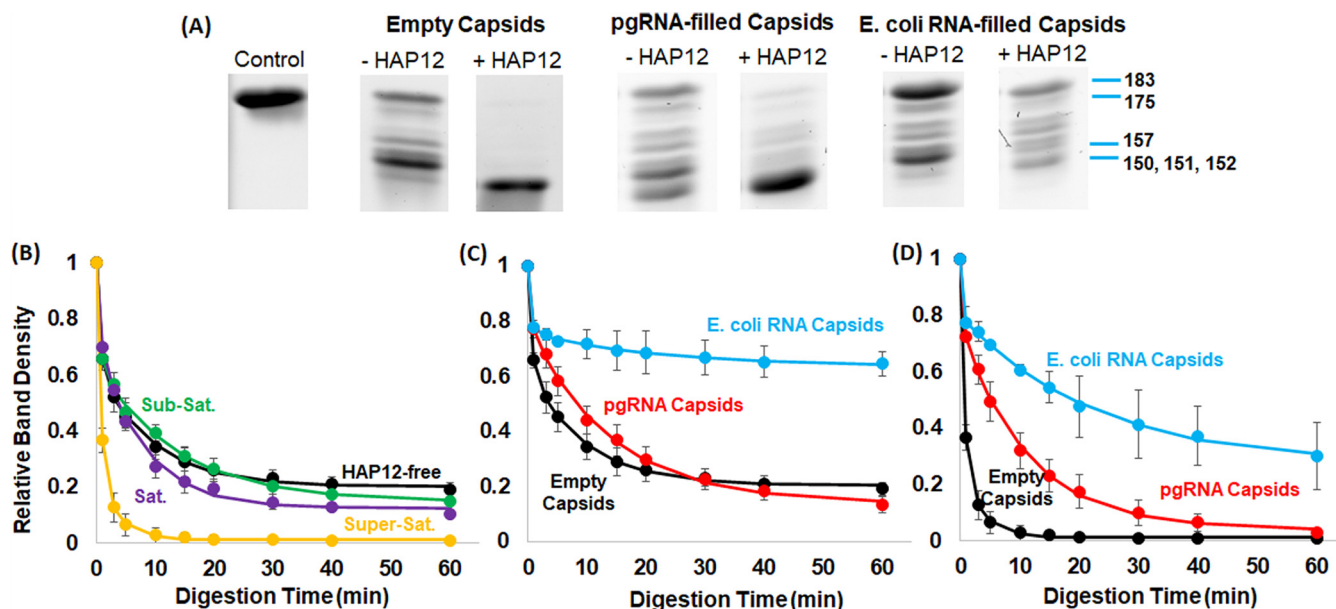


**FIG 2** Excess HAP12 changed the proteolysis pattern and led to faster and more complete proteolysis of CTDs. CTD exposure was measured as a function of trypsin digestion. Empty, pgRNA-filled, and *E. coli* RNA-filled capsids were treated with HAP12 and then exposed to trypsin at room temperature. Capsid and trypsin concentrations were  $7 \mu\text{M}$  and  $0.04 \mu\text{M}$ , respectively. Reactions were quenched by acidification and analyzed by SDS-PAGE and LC-MS. (A) SDS-PAGE of proteolyzed, drug-free capsids (-HAP12) and capsids treated with a supersaturating concentration of HAP12 (+HAP12) capsids. These samples were digested for 60 min. Prominent bands, identified by LC-MS, are labeled in the rightmost image. Untreated capsids retained substantive fractions of intact Cp183. With excess HAP12, the CTDs of empty and pgRNA-filled capsids were almost completely digested; *E. coli* RNA-filled capsids exhibited about equal distributions of different proteolyzed bands. (B to D) Time courses of cleavage at various HAP12 concentrations (B), various capsid contents (empty, pgRNA-filled, and *E. coli* RNA-filled) without HAP12 (C), and various capsid contents with supersaturating HAP12 (D). The relative band density is defined as the optical density of undigested Cp183 divided by the total optical density of the lane.

and CTDs would keep these flexible peptides inside (18). We also predicted that pgRNA capsids would become more susceptible to proteolysis after HAP12 treatment, based on our proteolysis results with empty capsids (Fig. 2A). For these experiments, purified Cp183 dimers were assembled with *in vitro*-transcribed pgRNA to produce RNA-filled capsids. In the absence of HAP12, pgRNA-filled capsids were slightly slower to show signs of proteolysis. However, the pgRNA-filled capsids yielded a cleavage pattern distinctly different from those of empty capsids (Fig. 2A). An important difference was that pgRNA-filled capsids had a prominent band for cleavage at residue 150, almost absent in empty capsids, suggesting that for at least a subset of subunits, the CTDs were more easily digested at the junction with the assembly domain. The pgRNA capsids also had a different relative distribution of the cleavage doublets. In the presence of supersaturating HAP12, pgRNA-filled capsids were more resistant to proteolysis than empty capsids, retaining small amounts of partially cleaved Cp183 after 1 h, but more sensitive to proteolysis than pgRNA-filled capsids without HAP (Fig. 2A).

As an alternative to *in vitro*-assembled pgRNA-filled capsids, we also tested *Escherichia coli* RNA-filled capsids. When expressed in *E. coli*, Cp183 dimers assemble around nonspecific *E. coli* RNA (20, 38, 39). For *E. coli* RNA-filled capsids in the absence of HAP12, the most prominent band after trypsin treatment remained intact Cp183, showing that these capsids were more resistant to proteolysis than empty and pgRNA-filled capsids (Fig. 2A). Digestion of *E. coli* RNA-filled capsids with supersaturating HAP12 produced almost equal distributions of each proteolysis product. The *E. coli* RNA capsids were much more resistant to trypsin than pgRNA-filled capsids. *E. coli* RNA-filled capsids had a larger population of uncleaved CTDs at 1 h (64% and 27%, respectively) than did pgRNA-filled capsids (14% and 4%, respectively) (Table 1). However, with no HAP12 or excess HAP12, both RNA capsids had similar fast-cleaving populations of  $22\% \pm 2\%$ , which is close to the 25% predicted for quasi-equivalence. The data suggest that a quasi-equivalent class of monomers is less protected by the internal RNA and more accessible for proteolysis.



The differences in cleavage pattern and extent suggested fundamental mechanistic differences in CTD exposure. To compare the differences, we measured the rates of loss of Cp183 for empty, pgRNA, and *E. coli* RNA capsids, with and without supersaturating concentrations of HAP12. On a relative scale, depending on the presence of HAP12, empty capsids exhibited the fastest hydrolysis, pgRNA-filled capsids showed an intermediate rate, and *E. coli* RNA-filled capsids had the slowest hydrolysis (Fig. 2B to D). In the absence of HAP12, digestion appeared to stall for all three capsid types tested. In the presence of supersaturating concentrations of HAP12, empty and pgRNA capsids lost approximately 100% of the initial Cp183 (Fig. 2D and Table 1). For *E. coli* RNA-filled capsids, CTDs were hydrolyzed slightly faster than in the absence of HAP12 but were still the slowest of the HAP-bound capsids; also, it was not clear whether digestion would proceed to completion with longer incubation. For both untreated and treated conditions, our data demonstrated that the RNA content of a capsid can modulate the kinetics of CTD exposure. However, the RNA-CTD interaction does not completely trap CTDs within the capsid and prevent exposure.

**HAP12 treatment causes capsid deformation.** Our proteolysis data indicated that HAP12 caused local structural changes that increased CTD exposure. To determine how these observations correlate with global changes in capsid morphology, we treated empty capsids with saturating HAP12 and examined them by negative-stain transmission electron microscopy (TEM). Previous work with HAP-TAMRA and Cp149 capsids showed that HAPs cause deformation of normal capsids (15); similar behavior was seen with a dibenzodiazepine CpAM (40). We anticipated that HAP12 treatment of empty Cp183 capsids would also lead to capsid deformation. Capsid samples were stained with ammonium molybdate and trehalose; trehalose was used to maintain the three-dimensional (3D) structure of capsids by minimizing the sample flattening that occurs when grids are dried. In representative micrographs, HAP-treated capsids show a relatively small number of divergences from control particles (Fig. 3A and B). 2D class averages tell a more detailed story. Class averages of untreated capsids showed nearly circular particle projections (Fig. 3C); this morphology is also seen in cryo-EM (15). Class averages of HAP12-treated capsids displayed distinctly deformed structures; capsids were faceted, elongated, and broken (Fig. 3D). Faceted and elongated capsids were the most common. The first 10 classes accounted for 92% of the images. It was not clear how their global structural changes affected local regions of the capsid and led to greater CTD mobility. The broken capsid classes, which accounted for only 4% of the images, showed unambiguously how internal CTDs could be probed by proteolysis. It is possible that local changes led to greater CTD exposure or that HAP treatment promoted transient ruptures. In addition, we noted that the asymmetry of these classes may explain why the populations from our proteolysis curve fitting (Table 1) were not consistent with quasi-equivalence.

**HAP12 with Imp $\beta$  led to disruption of empty capsids, but *E. coli* RNA-filled capsids appeared unperturbed.** The proteolysis data indicated that high HAP12 concentrations led to more CTD exposure in terms of the fraction of CTDs exposed, the length of the exposed peptide, and the rate of exposure. TEM data confirmed that HAP12 treatment causes capsid deformation, which correlates with greater CTD accessibility. This led us to question whether HAP12 treatment increased capsid binding to a biologically relevant ligand, the nuclear transport protein Imp $\beta$ , and whether the stress of two different capsid ligands, HAP12 and Imp $\beta$ , changed capsid integrity. Initially, we tested and confirmed Imp $\beta$  binding to empty capsids under HAP12-free and HAP12-treated conditions using size exclusion chromatography (SEC) and SDS-PAGE (Fig. 4A to C). To observe capsid morphology, untreated and HAP12-treated empty and *E. coli* RNA-filled capsids were mixed with Imp $\beta$ , dialyzed into low salt, and observed via negative-stain TEM. Control micrographs show that untreated capsids, empty and *E. coli* RNA filled, appeared spherical and intact (Fig. 5). Addition of Imp $\beta$  had little effect on capsid morphology. We observed a similar capsid morphology when subsaturating HAP12 and Imp $\beta$  were added to empty and *E. coli* RNA-filled capsids. However, we note that, at subsaturating HAP12, the capsid border appeared uneven and thicker

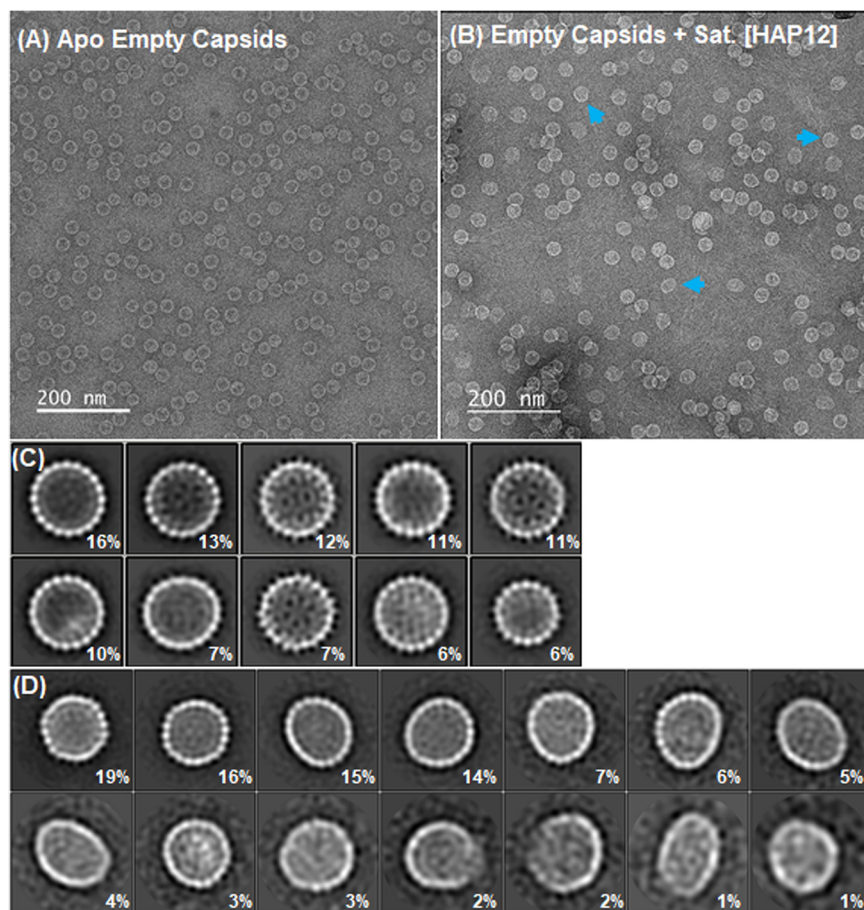


**FIG 3** HAP12 treatment causes capsid deformation. Untreated (A, C) and treated (B, D) empty capsids were compared by negative-stain EM. (A) A TEM of capsids with no HAP12 shows a narrow range of diversity. (B) A TEM of capsids in saturating HAP12 shows that damage to capsids is evident even without averaging. Blue arrows indicate deformed capsids. Samples were stained with ammonium molybdate, with trehalose added to minimize sample flattening and distortion due to drying. (C) Class averages of 5,307 nontreated-capsids from negative-stain TEM show a circular cross-section. (D) Class averages of 1,160 capsids treated for 2 h with saturating HAP12, at 25°C, show elliptical, faceted, and broken morphologies; capsid deformation by HAP12 is nearly universal but irregular. The population of each class is shown in the bottom right corner.

than those of nondrugged capsids. The thicker capsid shells may be due to bound Imp $\beta$ . The observation of thicker capsid walls made us curious if subsaturating HAP12 stabilized empty capsids, reduced the internalization of Imp $\beta$ , and led to more externally bound Imp $\beta$ . To test this, 2D class averages were generated to determine the morphologies of these capsids.

For empty capsids with Imp $\beta$ , based on class averages, 48% of particles showed visible, externally bound Imp $\beta$ , while 36% of particles showed no Imp $\beta$  (Fig. 6A). One class, accounting for 13% of particles, had density within the bounds of the capsid walls, suggesting internalized Imp $\beta$  as observed in earlier studies (26). It is possible that in classes without evident Imp $\beta$ , the importin adopted various conformations so that the signal was blurred into background during averaging. With Imp $\beta$  and subsaturating HAP12, 90% of empty capsids showed unambiguous, externally bound Imp $\beta$  (Fig. 5 insets and Fig. 6B). This observation suggests that these Imp $\beta$  proteins adopted similar localizations. The Imp $\beta$  density (“U” or “J” shaped) and arrangement were clear enough to allow us to determine the symmetry axis, based on the number of external Imp $\beta$  proteins in each class. Ten external Imp $\beta$  proteins separated at the same intervals on the particle surface suggested that we were looking down a 5-fold axis (Fig. 6B). Eight external Imp $\beta$  proteins suggested that we were peering down a 2-fold axis.

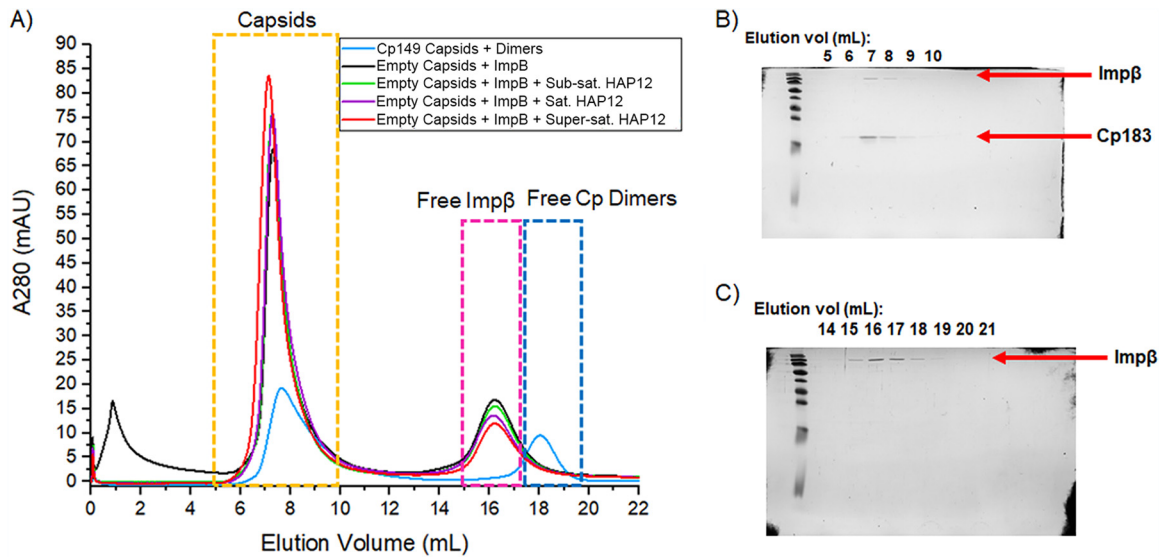


**FIG 4** SEC shows that supersaturating HAP12 led to elution of larger complexes. Impβ-bound capsids were resolved on a Superose 6 column and fractions were analyzed by SDS-PAGE. (A) In the compiled chromatographs, the capsid peaks were slightly shifted to the left with the addition of Impβ and increasing HAP12. A mixture of Cp149 capsids and dimers was run as a control to designate elution of capsids and dimers. The dashed-line boxes indicate the elution volumes for capsids (yellow), free Impβ (pink), and free dimers (blue). (B) The gel image shows co-elution of Cp183 and Impβ at 7 to 9 mL, indicating Impβ-bound capsids. (C) Free Impβ elutes at 15 to 19 mL.

Two classes, accounting for 7% and 2% of classified particles, had strong internal density, and two (17% and 10%) had internal U-shaped features that were suggestive of internalized Impβ but could also be CTDs (some of these observations are addressed in the charge detection mass spectrometry [CDMS] analysis below).

*E. coli* RNA-filled capsids appeared unperturbed and maintained a normal capsid morphology even with excess HAP12 (Fig. 5). 2D class averages of these samples confirmed

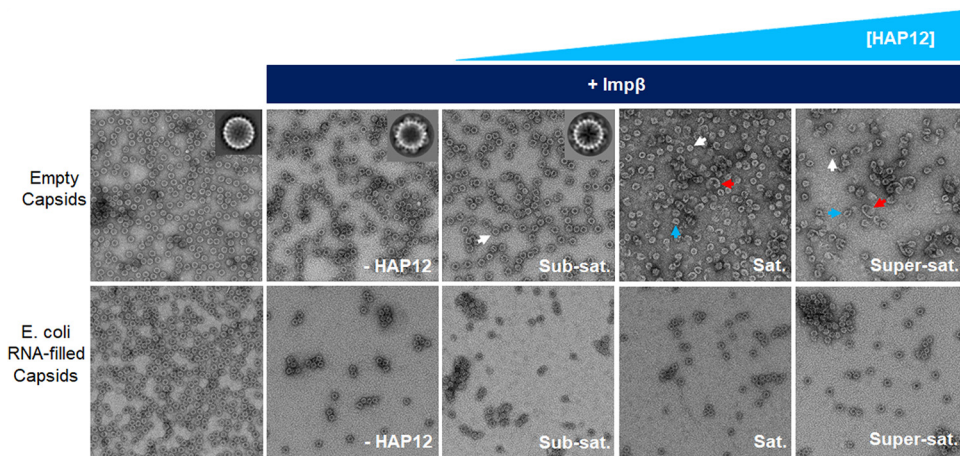


**FIG 5** HAP12 with Impβ led to disruption of empty capsids. Empty and *E. coli* RNA-filled capsids were mixed with Impβ so that there were 80 Impβ molecules per capsid (Cp183 dimer and Impβ concentrations were 11.9 μM and 8 μM, respectively), dialyzed into low salt (150 mM NaCl) to facilitate binding, and visualized by negative-stain TEM. Relative HAP12 concentrations are shown in white. Arrows highlight capsids of specified morphology as follows: white arrows, round, “normal,” capsids; blue arrows, deformed/intact capsids; and red arrows, broken capsids/aberrant structures. Drug-free empty capsids appeared spherical and intact, which is reflected in its representative 2D particle projection (inset). After the addition of Impβ, capsids with no HAP12 or subsaturating HAP12 concentrations similarly appeared round and intact; each has representative cross-sections that show well-ordered, external Impβ density (insets and Fig. 6). Introduction of Impβ and saturating or higher concentrations of HAP12 to empty capsids produced broken capsids and heterogenous complexes (Fig. 5). *E. coli* RNA-filled capsids remained morphologically unchanged, even with treatment with a high concentration of HAP12.



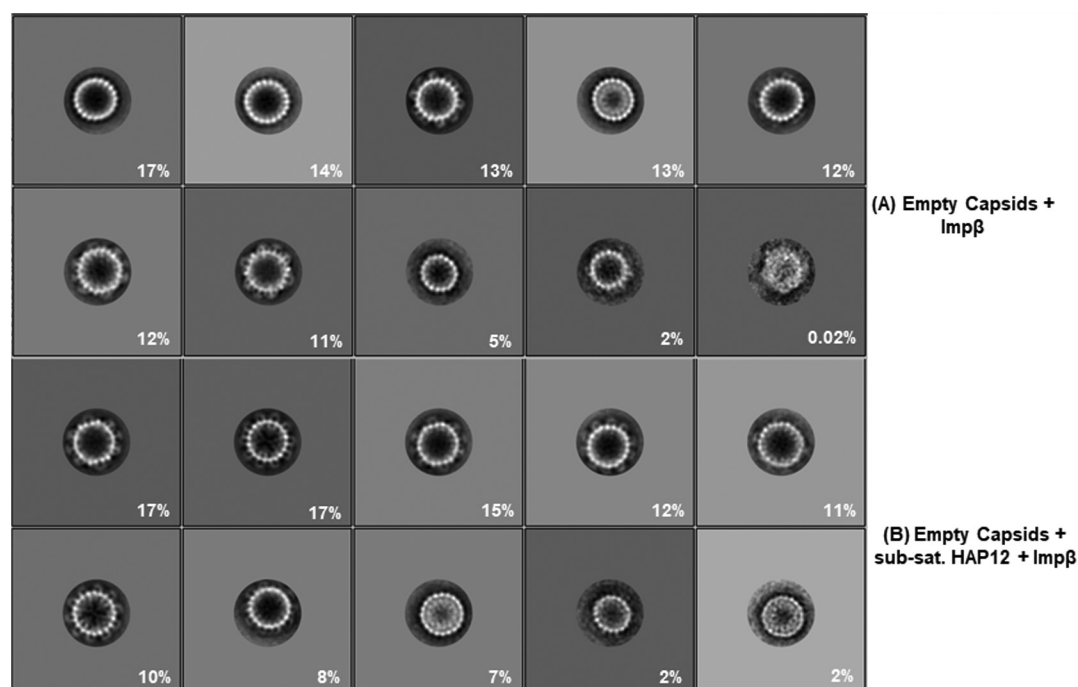


**FIG 6** Empty capsids treated with subsaturating HAP12 appeared to have more externally bound  $\text{Imp}\beta$  than drug-free capsids. (A and B) Class averages of HAP-free empty capsids plus  $\text{Imp}\beta$  (4,718 particles) and empty capsids plus subsaturating HAP12 plus  $\text{Imp}\beta$  (5,118 particles) were compared for differences in capsid morphology. (A) Empty capsids were prepared as previously stated in the legend for Fig. 5. HAP12-free empty capsids showed four classes (48% of total particles) with visible, externally bound  $\text{Imp}\beta$ . (B) However, capsids treated with subsaturating HAP12 showed seven classes (90% of total particles) with external  $\text{Imp}\beta$ . These observations suggested that substoichiometric HAP12 stabilized Cp-Cp interactions, preventing breakage of dimer-dimer contacts and internalization of  $\text{Imp}\beta$ .

that *E. coli* RNA capsids were able to maintain capsid geometry despite the presence of  $\text{Imp}\beta$  and superstoichiometric CpAM (Fig. 7B). It appears that the interaction between internal RNA and CTDs reduces all or most subunit modulation caused by HAP12 binding. However, we note that our proteolysis data still indicated that supersaturating HAP12 changed CTD exposure (Fig. 2 and Table 1).

When saturating or supersaturating HAP12 and  $\text{Imp}\beta$  were added, empty capsids became a heterogeneous population of spherical capsids, deformed but intact capsids, ruptured capsids, and large Cp oligomers. To avoid the artifacts of negative-stain TEM, we performed cryo-electron tomography to characterize the diverse population of deformed and disrupted particles. The tomograms showed new 3D structural features (Fig. 8). As with negative-stain TEM, we observed a range of Cp oligomers. The largest oligomers had clear regions of hexagonal patterning. We also observed areas of flat Cp sheets not seen in negative-stain images. Some sheets were relatively small and suggested a capsid that had unraveled in favor of planar geometry, leaving numerous gaps. Other oligomers were much larger than capsids, indicating that subunits, or oligomers of subunits, had been released and subsequently reassociated. The tomograms show how small molecules that impair Cp assembly also disrupt capsids and rearrange subunit geometry.

**CDMS of empty capsids with and without  $\text{Imp}\beta$  and with and without HAP12 showed shifts in mass and charge.** The combination of HAP12 and  $\text{Imp}\beta$  led to structural and physical-chemical changes to empty capsids. This suggested that HAP12-induced capsid deformation may influence the number of  $\text{Imp}\beta$  proteins binding to capsids. We predicted that saturating HAP12 treatment would allow more  $\text{Imp}\beta$  proteins to bind to capsids than to apo capsids and that greater  $\text{Imp}\beta$  binding would correlate with more capsid disruption. To measure the number of bound  $\text{Imp}\beta$  proteins, capsid complexes were analyzed by CDMS. CDMS measures the mass-to-charge ratio

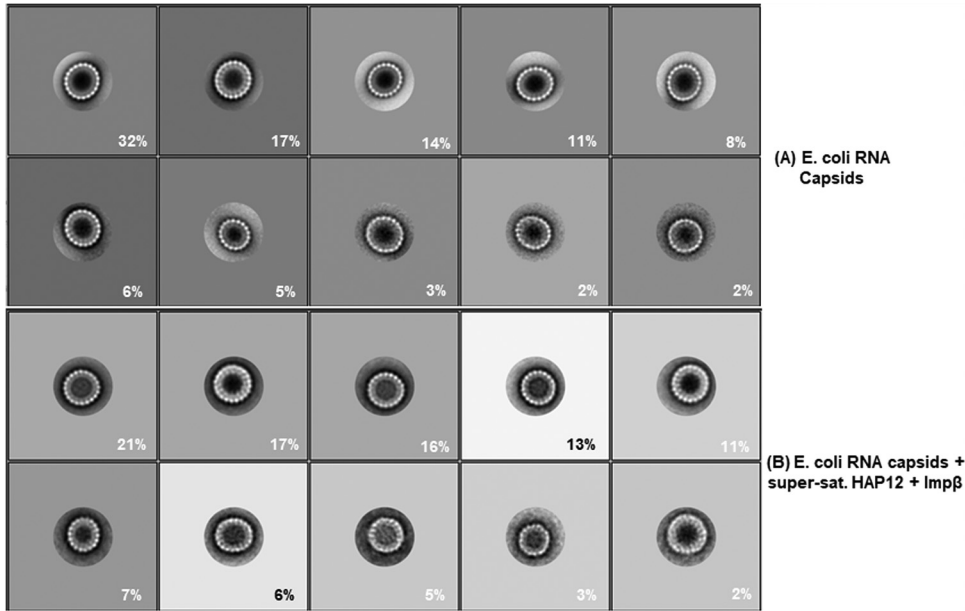


**FIG 7** After treatment with supersaturating HAP12 and Impβ, *E. coli* RNA-filled capsids appeared intact and spherical. (A and B) Class averages of *E. coli* RNA-filled capsids with no HAP12 (4,319 particles) or with supersaturating HAP12 plus Impβ (4,247 particles) were compared for differences in capsid morphology. (A) *E. coli* RNA capsids were prepared as previously stated in Fig. 5. Untreated *E. coli* RNA capsids appeared intact and round. (B) Similarly, *E. coli* RNA capsids treated with supersaturating HAP12 and Impβ also appeared to be intact and spherical, suggesting that internal RNA prevented capsid deformation and disruption.

(*m/z*) and charge (*z*) of each ion; these values are multiplied to give the mass of each ion, making it particularly powerful when the sample is heterogenous. The surface area of a particle dictates the number of charges on the ion; an approximation of the charge on a spherical water droplet, the Rayleigh limit, is a predictor for the number of charges on a spherical particle (41), while highly charged ions located above the limit are likely to have more extended or textured surfaces (42).

Empty capsids exhibited a narrow peak at 5.3 MDa, which is consistent with the mass expected for a T = 4 capsid (5.05 MDa) plus about 1% for counterions, salts, and

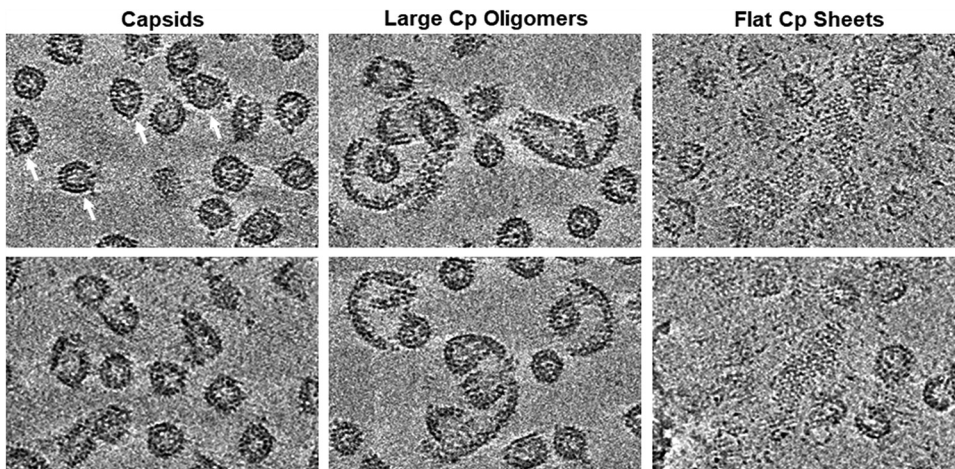


**FIG 8** Cryo-electron tomographs of Impβ and HAP12-bound empty capsids revealed a diverse group of particles and Cp oligomers. Selected slices from tomograms of capsids treated with saturating HAP12 (for 2 h) and Impβ (16 h) suggest a progression of events. Capsid-sized objects, some of which are clearly distorted and broken are the most common species (left column). Large Cp oligomers have many more dimers than a capsid and have a much larger radius of curvature (middle column). Flat Cp sheets are seen in some tomographic sections; these may result from a capsid unfurling or may result from free dimers self-assembling with planar geometry (right column).

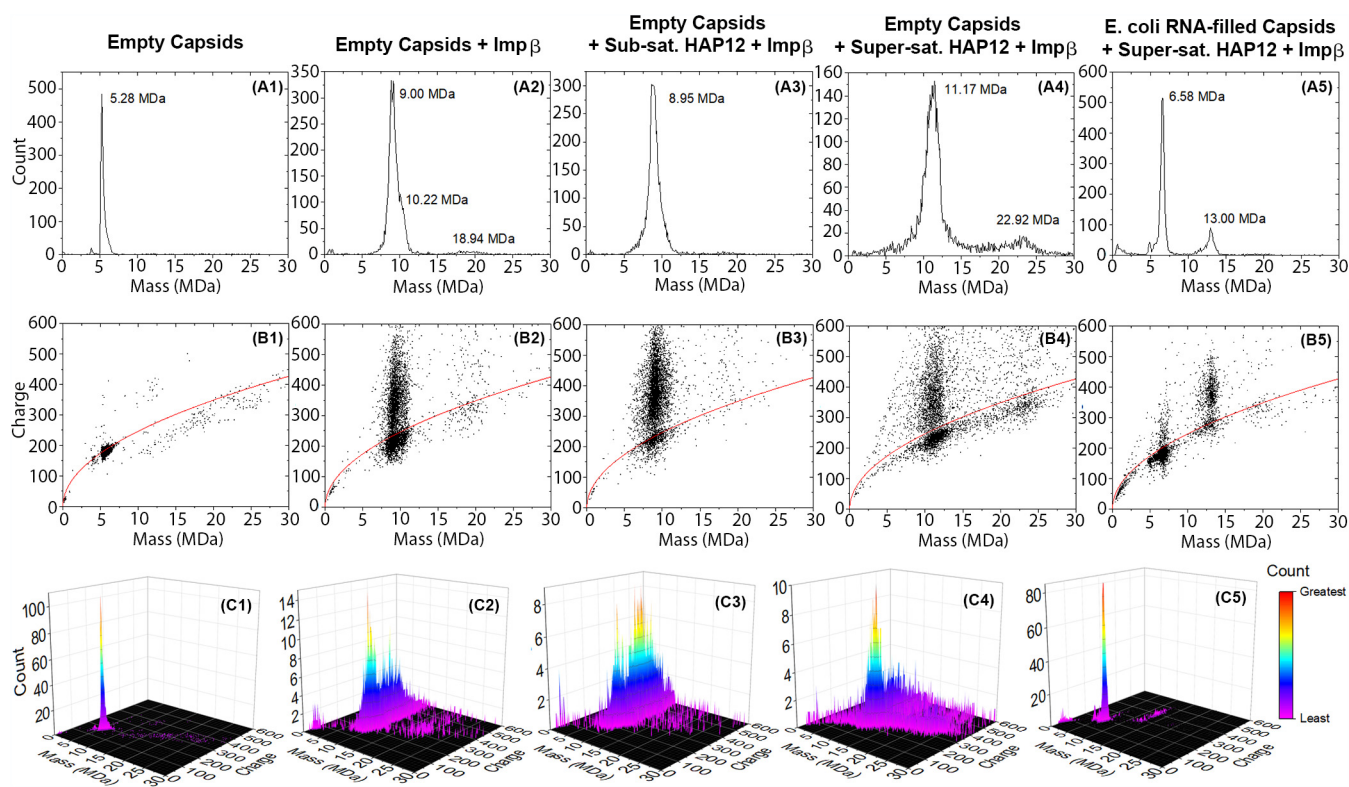


**FIG 9** CDMS of empty capsids with and without  $\text{Imp}\beta$  and with and without HAP12 showed shifts in mass and charge. (A1 to A5) Mass spectra; (B1 to B5) charge-versus-mass plots to identify individual ions (the Raleigh limit [red] shows the theoretical limit for the of charges on a spherical ion); (C1 to C5) 3D heat maps to identify distributions of populations. For empty capsids, mass shifts indicated  $\text{Imp}\beta$  binding to capsids. Most capsids showed two charged populations: a population near the Raleigh limit, suggesting spherical particles, and a second, more highly charged plume, suggesting extended or highly textured structures. Columns 1 to 4 show how empty capsids change mass and charge distributions in response to  $\text{Imp}\beta$  and/or HAP12. *E. coli* RNA-filled capsids (column 5) with and without  $\text{Imp}\beta$  and with and without HAP12 exhibited no significant changes in their mass spectra, charge-versus-mass plots, or 3D heatmaps.

water that remained closely associated with the particle (Fig. 9A1). In the charge-versus-mass plot, where each point represents an individual ion, we see that empty capsids were closely distributed along the Rayleigh limit (Fig. 9B1). The 3D heatmap gives a clearer and more quantitative view of the distribution of ions in terms of mass and charge (Fig. 9C1).

When  $\text{Imp}\beta$  is added to empty capsids, the mass peak shifts to 9.0 MDa, indicating a modal average of about 38  $\text{Imp}\beta$  molecules (97 kDa each) binding to each capsid (Fig. 9A2). The charge-versus-mass plot shows two main populations of ions: a distribution near the Rayleigh limit and a vertical plume extending away from the limit (Fig. 9B2). The charge plot suggests that this sample contained both compact spherical particles and extended or more textured particles. As the corresponding TEM data showed no broken capsids or other extended structures, we suggest that the highly charged distribution was attributed to  $\text{Imp}\beta$ -decorated capsids, which would be highly textured and could accept more charge. The 3D heatmap revealed that most of the ions were spherical (Fig. 9C2). When subsaturating HAP12 and  $\text{Imp}\beta$  were added, a similar mass was detected at 8.95 MDa, also corresponding to 38  $\text{Imp}\beta$  proteins per capsid (Fig. 9A3). However, unlike with the sample without HAP12, the 3D heatmap indicated that subsaturating HAP12 led to more ions in the plume than in the cluster (Fig. 9C3). This observation and the previous 2D class averages indicated to us that adding substoichiometric HAP12 to empty capsids led to more externally bound  $\text{Imp}\beta$ . As a working hypothesis, in the absence of HAP12 and when a CTD binds  $\text{Imp}\beta$ , the capsid may internalize the host protein to relieve some of the mechanical strain on the capsid. However, with subsaturating HAP12, CpAMs can strengthen Cp-Cp contacts and consequently suppress transient ruptures so that bound  $\text{Imp}\beta$  remains outside.



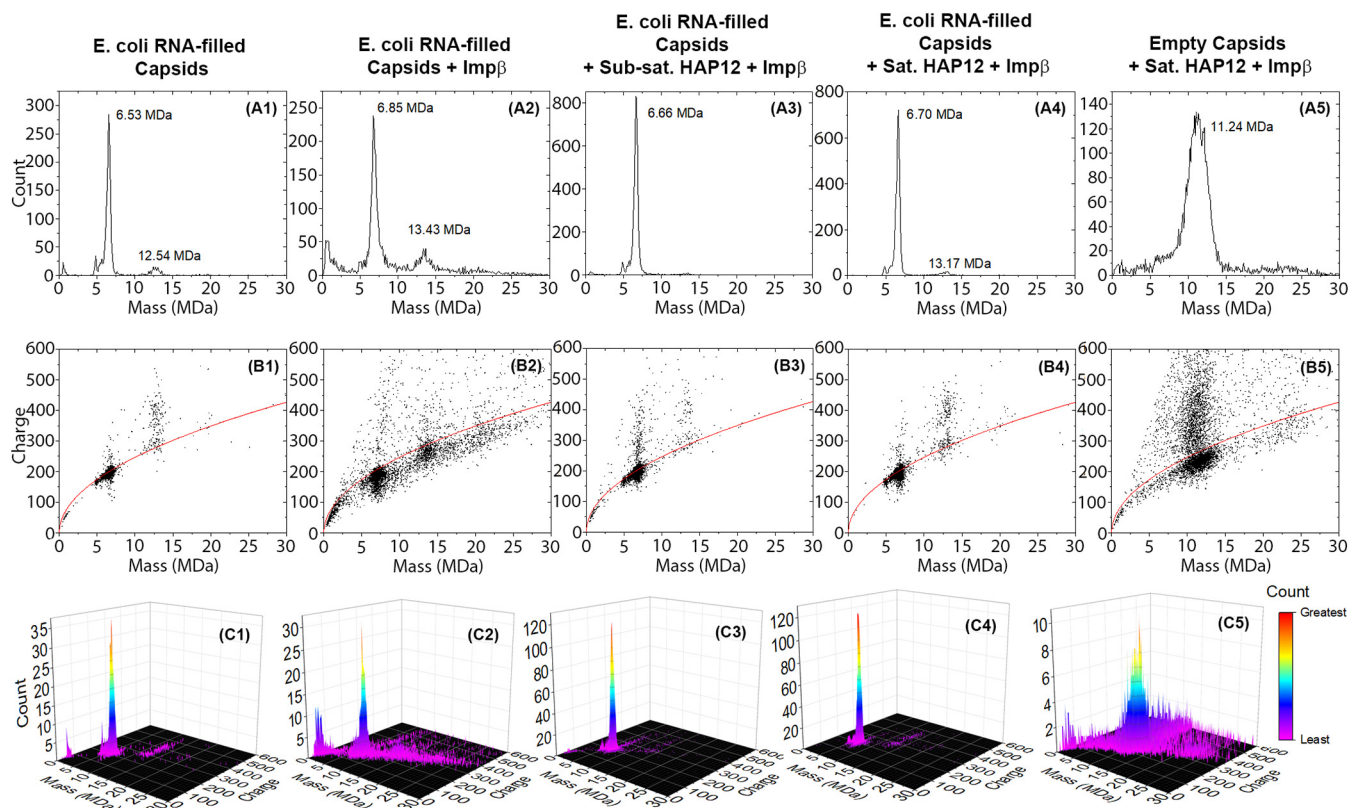


**FIG 10** CDMS of *E. coli* RNA-filled capsids with and without *Impβ* and with and without HAP12 showed no significant shifts in mass and charge. (A1 to A5) mass spectra; (B1 to B5) charge-versus-mass plots with Rayleigh limit (red curve); (C1 to C5) 3D heatmaps. For *E. coli* RNA-filled capsids, no mass shifts were observed despite the addition of *Impβ* or HAP12. For all *E. coli* RNA capsid samples, a concentration of ions was detected along the Rayleigh limit, suggesting spherical capsids. The 3D heatmaps show that *E. coli* RNA capsids fall into a single population of ions. Conversely, after addition of saturating HAP12 and *Impβ*, empty capsids undergo a mass shift and ion population changes that are similar to those of empty capsids treated with supersaturating HAP12 (Fig. 9).

Supersaturating HAP12 and *Impβ* led to a shift in mass to 11.2 MDa, corresponding to approximately 64 *Impβ* proteins per capsid (Fig. 9A4). We also observed the presence of many small and large ions, suggesting that some capsids had fragmented and some Cp183 dimers had coalesced into larger complexes (Fig. 5 and 9A4). This is consistent with tomographic data showing loosely connected sheets of protein and free subunits rearranging to create new structures (Fig. 8). Of note, we observed a small broad peak at 22.92 MDa, which may be a dimer of two capsids; examination of the other mass spectra showed the same double capsid peak. Most of the ions attributed to capsids with *Impβ* and supersaturating HAP12 were near the Rayleigh limit, suggesting that most had a spherical morphology (Fig. 9B4 and C4). The corresponding TEM images showed many normal-sized particles and a heterogeneous population of large oligomers (Fig. 5). We also note that the addition of saturating HAP12 produced mass and charge results similar to those seen in the supersaturating HAP12 samples (Fig. 10A5, B5, and C5).

While empty capsids showed evidence of CTD exposure and capsid deformation, at supersaturating HAP12, CDMS of *E. coli* RNA-filled capsids exhibited no mass shifts (Fig. 9A5). Independently of all HAP12 concentrations, the peak attributed to *E. coli* RNA-filled capsids ranged from ~6.5 to 6.9 MDa, indicating little-to-no *Impβ* binding (Fig. 9A5 and Fig. 10A1 to C4). This ~1.4-MDa mass difference from that of an empty capsid is attributable to about 4,200 nucleotides of RNA. Most of the ions were near the Rayleigh limit, suggesting intact round capsids (Fig. 9B5 and Fig. 10B1 to B4).

## DISCUSSION

Our study shows that exogenous molecules can work synergistically to disrupt HBV capsids. HAP12 globally disrupts capsid geometry and also modulates the accessibility of



CTDs. CTD mobility and capsid stability are differentially modulated, depending on the saturation of HAP sites. At low HAP12 saturation, CTD exposure remains unchanged from that of an unmodified capsid, but capsids appear to be more stable. At saturating or excess HAP12, CTD accessibility to protease increases, and capsids become disrupted with the addition of Imp $\beta$ s. Additionally, encapsidated RNA modulates CTD exposure and increases capsid stability. *E. coli* RNA-filled capsids did not experience significant HAP-induced changes to their capsid geometry, as was observed with empty capsids. The RNA content of these capsids appeared to protect them against disruption. Though we were unable to test the sensitivity of a mature double-stranded DNA (dsDNA)-filled capsid to CpAMs and Imp $\beta$ , the predicted and observed fragility of these particles (43, 44) led us to predict that they are about as sensitive to disruption as empty particles.

This work shows that Cp-Cp interactions and consequently capsid stability can be exploited by small molecules. Like other CpAMs, HAPs exert seemingly paradoxical effects when bound to HBV capsids (16, 17). These small molecules increase the association energy of interdimer contacts (13, 15). However, by locally distorting the interdimer interface, HAPs can disturb global icosahedral geometry (15–17, 40, 45, 46). As more HAPs bind, a global cascading effect on capsid structure leads to deformation and eventually disruption (14–17, 40). HAP12 concentration also differentially affects CTD and capsid dynamics. In a T = 4 capsid, there are A, B, C, and D pockets, each capped by a neighboring subunit. HAPs preferentially bind B and C sites; A and D sites are sterically hindered (see Fig. 3a in reference 40). Under subsaturating conditions, when HAP fills B and C sites, capsids are stabilized (13). We observe that when there is enough HAP to fill all four classes of site, capsids are destabilized because HAPs disrupt icosahedral geometry (14, 40). We showed that untreated or subsaturating HAP12 conditions do not increase CTD sensitivity to protease activity in empty capsids. CTD accessibility increases only when HAPs reach a concentration threshold of saturating or higher. Therefore, Cp-Cp interactions experience a local stabilizing effect and global destabilizing effects from HAPs, depending on concentration; CTD mobility is not directly affected by CpAMs.

The stabilizing and destabilizing effects of CpAMs can be exacerbated by Imp $\beta$ . At subsaturating HAP12, empty capsids do not show deformation but exhibit more externally bound Imp $\beta$  than seen with undrugged empty capsids. This assertion is based on CDMS data showing that the supersaturating HAP12 and supersaturating Imp $\beta$  empty particles have a larger population of ions with a charge in excess of the Rayleigh limit than the subsaturating HAP12 particles, suggesting that the supersaturating HAP12 particles have more textured surfaces (Fig. 9C2 and C3). This observation is consistent with a subsaturating HAP12, bound at a subset of pockets, that strengthens dimer-dimer interactions to prevent capsids from transiently breaking and internalizing bound Imp $\beta$ s (26). In addition, externally bound importins may further stabilize the capsids by neutralizing some of the positive charges at CTD clusters around the quasi-6-fold vertices (18). When we add saturating or supersaturating HAP12 along with Imp $\beta$ , empty capsids deform, disrupt, and form Cp oligomers. Even though CpAMs strengthen interdimer contacts, it is not enough to offset the perturbation to capsid geometry which results in rearrangement of subunits. In addition to the effect of the CpAMs, the Imp $\beta$  binding site extends beyond the CTD, which may exert a “pulling” force, partially unfold the dimer, or generally disturb the capsid’s quaternary structure (26). This interaction further compounds the mechanical strain on the capsid.

Nucleic acid also impacts CTD and capsid molecular motion. Internal RNA influences the organization of CTDs (18). Here, we observed that differences in RNA content affect capsid behavior. In this study, we observed that CTD exposure was slower with both RNA capsid types that were tested. Surprisingly, pgRNA-filled capsids were much more protease sensitive than *E. coli* RNA-filled capsids. Similarly, our data indicated that no Imp $\beta$  bound to *E. coli* RNA-filled capsids (Fig. 9A5, B5, and C5; Fig. 10A1 to C4), despite the presence of excess HAPs and CTD accessibility to proteases (Fig. 2A to D and Table 1). This lack of binding to *E. coli* RNA-filled capsid was also observed with serine-arginine protein kinases (25). We surmise that electrostatic RNA-CTD interactions inhibit

CTDs from externalizing to the capsid exterior. We also observed that *E. coli* RNA capsids do not experience detectable capsid deformation after treatment with excess HAP12 (Fig. 5). We suggest that CTDs electrostatically cross-link dimers via their interaction with packaged nucleic acid to overcome capsid distortion.

Although RNA-filled capsids appeared more stable than empty capsids, their stabilities were further differentiated by their net internal charges. Our pgRNA-filled capsids have a net +200 charge: −3,200 for the RNA and +3,360 for the CTDs (+14 per Cp monomer from 16 arginines, one glutamate, and the C terminus). Based on our CDMS data, the *E. coli* RNA-filled capsids used in these experiments have about 1.4 MDa of RNA, about 4,200 nucleotides from an undetermined number of polynucleotides, resulting in a net −840 charge (Fig. 9A5, B5, and C5 and Fig. 10A1 to C4). With or without excess HAP12, pgRNA capsids showed more cleavage than *E. coli* RNA capsids (Fig. 2A to D and Table 1). The excess positive charge of pgRNA-filled capsids indicates that not all CTDs can be protected. Furthermore, the single long pgRNA may have limited access to CTDs (47); pgRNA is just long enough to coat the interior surface of the capsid (48). Conversely, the packaged *E. coli* RNA is present in shorter and longer sizes that can avoid the constraints of a single polynucleotide (19, 47, 49).

We propose that HAP12 and Imp $\beta$  can strain a capsid and that above a threshold of strain, a ruptured capsid is more stable than an intact one, an accumulated strain model applied to icosahedral viruses (40, 50). We propose that the free energies of a HAP12 and Imp $\beta$ -bound capsid in its strained (equation 1) and ruptured states (equation 2) are defined as follows:

$$\Delta G_{\text{strained}} = N\Delta G_{\text{cont}} + P_{\text{sites}}\Delta G_{\text{HAP12}} + X_{\text{Imp}\beta}\Delta G_{\text{Imp}\beta} + (C_{\text{HAP12}}\Delta G_{\text{strain, HAP12}} + C_{\text{Imp}\beta}\Delta G_{\text{strain Imp}\beta}) \quad (1)$$

$$\Delta G_{\text{ruptured}} = (N - N_{\text{broken}})\Delta G_{\text{cont}} + (P_{\text{sites}} - P_{\text{broken}})\Delta G_{\text{HAP12}} + (X_{\text{Imp}\beta} - X_{\text{broken}})\Delta G_{\text{Imp}\beta} + (C_{\text{HAP12}}\Delta G_{\text{strain, HAP12}} + C_{\text{Imp}\beta}\Delta G_{\text{strain Imp}\beta}) \quad (2)$$

First, consider an intact capsid (equation 2).  $N$  accounts for the 240 contacts made by the 120 dimers in a  $T = 4$  capsid. Based on structures of capsids with bound HAPs (15, 46), we assume that HAP12 binds to the 120 B and C sites in a  $T = 4$  capsid, noted as  $P_{\text{sites}}$  (15, 46); HAP bound to the 120 disfavored (and destabilizing) A and D sites is accounted for by  $\Delta G_{\text{strain, HAP12}}$ . The values for  $\Delta G_{\text{cont}}$ , where “cont” is “contact,” and  $\Delta G_{\text{HAP12}}$  are  $-3.1 \text{ kcal} \cdot \text{mol}^{-1}$  and  $-1.9 \text{ kcal} \cdot \text{mol}^{-1}$  per contact, respectively.  $\Delta G_{\text{Imp}\beta}$  is the increment that a bound Imp $\beta$  stabilizes a capsid, presumably by neutralizing some electrostatic repulsions of the CTDs; empty capsids disassemble and precipitate in the absence of excess ionic strength (28) or Imp $\beta$ .  $X_{\text{Imp}\beta}$  is the number of bound Imp $\beta$  molecules and is less than or equal to 240. Finally, in an intact capsid, there are strain terms attributable to excess bound HAP (accounting for geometric effects and binding to disfavored sites) and Imp $\beta$ .

A ruptured capsid loses stabilizing and destabilizing energy to reach a minimum (equation 2).  $N_{\text{broken}}$  represents contacts that are lost after capsids rupture.  $P_{\text{broken}}$  accounts for lost HAP12 molecules that were initially bound at interdimer interfaces but are released once their contacts break.  $X_{\text{broken}}$  represents Imp $\beta$ -bound dimers that have disassociated after rupture. Finally, strain is lost;  $\Delta G_{\text{strain, HAP12}}$  and  $\Delta G_{\text{strain, Imp}\beta}$  are influenced by capsid deformation, so they are multiplied by the coefficients  $C_{\text{HAP12}}$  and  $C_{\text{Imp}\beta}$ , respectively. These strain coefficients range from 0 to 1 and increase nonlinearly as the HAP12 and/or Imp $\beta$  binding rises.

With subsaturating HAP12, icosahedral capsids are favored:  $\Delta G_{\text{strained}} < \Delta G_{\text{ruptured}}$  (Fig. 11B and D). However, at saturating and supersaturating HAP12,  $\Delta G_{\text{strain, HAP12}}$  is large, and capsids undergo disruption to relax that strain (Fig. 5 and 11E). An identical argument holds with high Imp $\beta$  binding. Under conditions where rupture is favored, the two  $C$  coefficients should be close to 0, so that  $C_{\text{HAP12}}\Delta G_{\text{strain, HAP12}}$  and  $C_{\text{Imp}\beta}\Delta G_{\text{strain, Imp}\beta}$  are relaxed. Saturating HAP12 or above is required to disturb capsid geometry and generate  $\Delta G_{\text{strain, HAP12}}$  (Fig. 11B). The addition of Imp $\beta$  compounds the capsid's already strained state further and drives the reaction to the ruptured state (Fig. 11F).

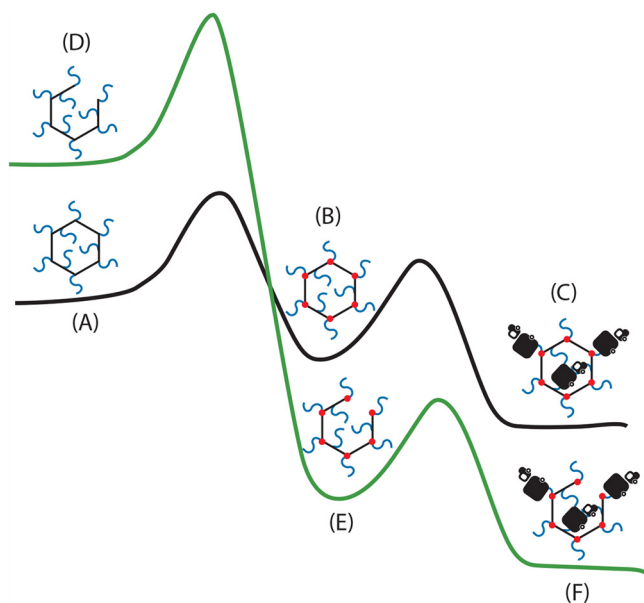


**FIG 11** Free-energy diagram of an empty capsid in its strained (A to C, black line) and ruptured (D to F, green line) states mediated by HAP12 and Imp $\beta$ . Because it has fewer interdimer contacts, an untreated, ruptured capsid (D) is in a higher energy state than that of an intact, drug-free capsid (A). (B) After enough HAP molecules (red dots) bind to cause capsid deformation, the strained, intact capsid pays a global strain penalty and is at a higher energy level. (E) By rupturing, a HAP-bound capsid relieves the global strain and achieves a lower energy state. Although Imp $\beta$  binding (black trucks) provides some stability to capsids, this interaction applies further mechanical strain to the capsid (C), which can be energetically compensated for by rupturing (F).

This paper demonstrates and analyzes the dual antiviral activities of CpAMs and their synergism with host proteins. Molecules like CpAMs have been documented for their ability to modulate capsid assembly, but their ability to disrupt capsids has been only implicit until recently (13–15, 40, 46, 52). Here, we also show that host proteins, in particular, Imp $\beta$ , can contribute to capsid disruption. Destabilizing a capsid adds to the arsenal of mechanisms of action for small-molecule HBV therapeutics. During the HBV life cycle, empty and rcDNA-filled capsids interact with host importins and are trafficked to the nucleus (53). When capsids enter the nuclear pore complex, capsid protein will interact with Nup153, which may facilitate uncoating (32). Capsid disassembly at inopportune times can impair the virus's ability to establish infection (16, 17). Furthermore, if rcDNA-containing capsids disassemble in the cytoplasm, the exposed viral DNA may be detected by the host's innate immune system (e.g., cyclic GMP-AMP synthase-stimulator of interferon genes, known as cGAS-STING [54]). Indeed, rcDNA capsids are fragile and may be particularly sensitive to disruption (43, 44, 55). Because Cp is involved throughout the HBV life cycle, CpAMs continue to be versatile and attractive candidates for developing an efficacious cure for chronic HBV infection.

## MATERIALS AND METHODS

**Protein purification and preparation.** *E. coli* RNA-filled Cp183 capsids were expressed and purified as previously described (28). To isolate Cp183 for subsequent experiments, *E. coli* RNA-filled Cp183 capsids were dialyzed in 1.5 M guanidine hydrochloride, 0.5 M LiCl, 10 mM dithiothreitol (DTT), and 20 mM Tris-HCl, pH 7.5 (disassembly buffer), at 4°C overnight. The sample was centrifuged at  $7,000 \times g$  for 10 min to pellet the RNA. Cp183 dimers were purified from the supernatant using a Superose 6 column (GE) equilibrated in disassembly buffer. To assemble empty capsids, dimers were dialyzed in 0.45 M NaCl, 10 mM DTT, and 20 mM Tris-HCl, pH 7.5 (assembly buffer), at 4°C overnight. To remove unassembled dimers, empty capsids were purified via size exclusion chromatography (SEC) with a Superose 6 column that was equilibrated with assembly buffer. To prepare pregenomic RNA (pgRNA)-filled Cp183 capsids, pgRNA was *in vitro* transcribed using the MegaScript kit (ThermoFisher) with plasmid 1135 (38), which was modified to have a T7 promoter. The modified plasmid 1135 was a gift from Dan Loeb. To assemble pgRNA-filled capsids, dimers and pgRNA were mixed in a 120:1 molar ratio and then dialyzed in 0.15 M NaCl, 10 mM DTT, and 20 mM Tris-HCl, pH 7.5, at 4°C overnight. To produce *E. coli* RNA-filled

capsids, stock *E. coli* RNA capsids were loaded onto a 10-to-40% continuous sucrose gradient and centrifuged at 40,000 rpm for 5 h; the capsid band was extracted and dialyzed into assembly buffer. Imp $\beta$  expression and purification protocols were adapted from the work of Chen et al. (26).

**Treatment of HBV capsids with the CpAM HAP12.** For HAP12 treatment, empty and pgRNA-filled capsids were incubated with HAP12 for 2 h away from light before they were used for experiments. To prepare drug stock samples, HAP12 was resuspended in 100% dimethyl sulfoxide (DMSO). HAP12 stocks contain a racemic mixture of 50% active and 50% inactive molecules; we always refer to HAP12 concentrations in terms of the whole racemic mixture. These concentrations correspond to the following HAP12-to-dimer molar ratios: 2:1, 4:1, and 8:1, respectively. For example, at saturating concentration, there would be 4 HAP12 molecules for every 1 dimer, which corresponds to 1 active HAP12 molecule per pocket. For control samples, capsid samples were incubated with DMSO.

**Proteolysis of HBV capsids.** The limited proteolysis assay performed in this paper was adapted from an assay in a previously published work (28). Reaction samples with empty, pgRNA-filled, and *E. coli* RNA-filled capsids were diluted in 0.5 mM NaCl, 10 mM  $\beta$ -mercaptoethanol, and 80 mM Tris-HCl, pH 7.5, and incubated with 0.04  $\mu$ M sequence-grade modified trypsin (Promega) for specific times. Proteolysis was quenched with 4 $\times$  Laemmli buffer and heating at 95°C for 6 min. Samples were then analyzed by SDS-PAGE on a 20% denaturing polyacrylamide gel, containing 0.4% (vol/vol) 2,2,2-trichloroethanol (TCE) to support direct fluorescent detection of protein samples (56). Gels were imaged with a ChemiDoc imager (Bio-Rad). Protein bands were quantified using the Fiji software (57). Each data point is the average of results from three independent trials, with a corresponding error bar. Curve fitting for CTD exposure kinetics was performed using the Solver function in Excel. For liquid chromatography-mass spectrometry (LC-MS), reactions were quenched by the addition of glacial acetic acid.

**LC-MS of proteolyzed Cp183.** Two separate LC-MS methods were used to characterize the peptides generated in the limited proteolysis experiments. The first focused on peptides with a molecular weight of less than 3 kDa. Before analysis, samples with peptides were passed through a 3-kDa-molecular-weight-cutoff filter (PALL) to remove larger peptides and undigested protein. The final concentration of peptides was approximately 0.1 mg/mL. One microliter of the peptide mixture was injected onto a Dionex 3000 nano-high-performance LC (HPLC) (ThermoFisher) coupled to a maXis Impact quadrupole time of flight (QTOF) mass spectrometer (Bruker Daltonics). Nano LC-tandem MS (MS/MS) analysis was performed as previously described. (58, 59). Briefly, LC was carried out using an Acclaim PepMap C<sub>18</sub> reverse-phase column (300  $\mu$ m by 5 mm) using a slow gradient: 0 to 2.5 min, 3% B; 2.5 to 20 min, 3 to 30% B; 20 to 23 min, 30 to 80% B; 23 to 25 min, 80% B; 25 to 28 min, 80 to 3% B; and 28 to 30 min, 3% B, where solvent A is 0.1% formic acid (FA; Sigma) in water (ThermoFisher) and solvent B is 0.1% FA in acetonitrile (ThermoFisher). The peptides were analyzed using PeptideShaker (60) coupled to SearchGUI (61).

LC-MS of peptides greater than 3 kDa was performed using an Agilent 1290 ultrahigh-performance LC (UPLC) series liquid chromatograph coupled to a micrOTOF (Bruker Daltonics). Ten microliters of the peptide mixture at approximately 0.1 mg/mL was injected onto the LC. The LC was carried out using a Phenomenex Onyx Monolithic C<sub>18</sub> reverse-phase column (100 by 2 mm) at 50°C, with a flow rate of 400  $\mu$ L/min. The following gradient was used: 1.0 min, 10% B; 1.0 to 8.0 min, 10 to 70% B; 8.0 to 8.5 min, 70 to 90% B; 8.5 to 9.0 min, 90 to 10% B; and 9.0 to 10.0 min, 10% B, where solvent A is 0.1% FA (Sigma) in water (ThermoFisher) and solvent B is 0.1% FA in acetonitrile (ThermoFisher). MS settings were as follows: the nebulizer was set to 5.0 bar, the drying gas was set at 7.0 L/min, the drying temperature was set at 200°C, and the capillary voltage was set at 4.5 kV. The capillary exit was set at 100 V, the skimmer 1 at 50 V, the hexapole 1 at 23 V, the hexapole RF at a 300 peak-to-peak voltage (Vpp), and skimmer 2 at 22 V. Data analysis was carried out using Bruker DataAnalysis with maximum entropy.

**HBV capsid and importin  $\beta$  binding experiments.** Imp $\beta$  was passed through a Superose 6 column to exchange the buffer into 0.5 M NaCl, 10 mM DTT, and 20 mM Tris-HCl, pH 7.5. Empty and *E. coli* RNA-filled capsids were mixed with Imp $\beta$  in a 1:80 ratio. Then, these samples were dialyzed into 0.15 M NaCl, 10 mM DTT, and 20 mM Tris-HCl, pH 7.5, at 4°C overnight to allow binding. The resulting complexes were analyzed via SEC, SDS-PAGE, CDMS, and TEM. For SEC, complexes were resolved using a Superose 6 column, and the overnight dialysis buffer was the running buffer. SDS-PAGE was performed with a denaturing polyacrylamide gel (4% stacking and 16% resolving).

**Transmission electron microscopy.** For negative-stain TEM of empty capsid morphology, capsids were mixed with 6% (wt/vol) ammonium molybdate and 0.5% (wt/vol) Trehalose and applied to glow-discharged continuous-carbon grids. For studies where sample flattening was not critical, samples were first applied to grids and then stained with 0.45% (wt/vol) uranyl formate or 2% (wt/vol) uranyl acetate. All grids were imaged using the JEOL 1400 FS microscope at 120 kV and at a magnification of  $\times$ 50,000.

**Cryo-electron tomography.** To prepare cryo-EM specimens, a drop of 4  $\mu$ l of the sample mixture was applied to a glow-discharged 300 mesh Quantifoil R2/2 holey carbon grid. The grid was plunged into a liquid ethane bath cooled by liquid nitrogen, using a ThermoFisher Scientific (TFS) Vitrobot Mark IV. The frozen hydrated cryo-EM grid was clipped into a cartridge and then transferred into a cassette before being loaded into a TFS 300-kV Titan Krios equipped with a Gatan BioContinuum energy filter, using a K3 direct electron detector camera. Data collection was set up using TFS Tomography software (v 4) under counting mode. The nominal magnification was  $\times$ 53,000 (equal to 1.7 Å per pixel), and the illumination had a dose rate of 0.7 e $^{-}$ /Å<sup>2</sup>. The zero-loss peak was aligned for each tilt series, using an energy slit of 20 eV. Tilt series were acquired using a bidirectional scheme from  $-60^\circ$  to  $60^\circ$ , with the tilt step at  $2^\circ$ . Therefore, the total accumulated dose is  $\sim$ 42.7 e $^{-}$ /Å<sup>2</sup>. Tilt series alignment, contrast transfer function correction, and tomogram reconstruction were performed using IMOD (v 4.9.12) (62). The final 3D reconstruction was generated with data binned at 4. Nonlinear anisotropic diffusion was applied to the final reconstruction to reduce noise (63).



**CDMS.** Charge detection mass spectrometry (CDMS) is a single-particle technique in which the mass-to-charge ratio ( $m/z$ ) and charge ( $z$ ) of each ion are measured simultaneously. Multiplying the  $m/z$  by the charge gives the mass of an ion. Measurements are performed on many individual ions to generate a mass distribution. This allows molecular weight distributions to be measured for large (>1-MDa) and heterogeneous species. These species cannot usually be analyzed with traditional mass spectrometry methods that have an effective upper limit of about 1 MDa. In this work, a home-built CDMS instrument, described previously (64–66), was used. Briefly, the analyte is ionized by a nano-electrospray source (Advion TriVersa NanoMate). The ions enter the instrument through a metal capillary and pass through three regions of differential pumping. They are then focused into a dual hemispherical deflection energy analyzer which transmits a narrow band of ion energies centered around the nominal ion energy of 100 eV/charge. The transmitted ions are focused into an electrostatic linear ion trap, where they are trapped when potential barriers are raised at both ends. As the ion oscillates back and forth in the trap, it passes through a conducting cylinder. The ion induces equal but opposite charges on this cylinder; the signal from the induced charge is amplified, digitized, and analyzed by fast Fourier transforms (66). The fundamental frequency is proportional to the  $m/z$  of the ion, while the amplitude of the signal is proportional to the charge of the ion. All mass spectra were generated using a 100-ms trapping time. Typical spectra contain thousands of individual ion measurements and take 30 to 50 min to collect. Before CDMS analysis, empty and *E. coli* RNA-filled capsid samples were buffer exchanged into a volatile buffer, 150 mM ammonium formate, pH 7.5, at 4°C. The CDMS data presented in this work include mass spectra, charge-versus-mass plots, and 3D heatmaps. In addition, all charge-versus-mass plots contained Rayleigh limit curves. The Rayleigh limit is a model that predicts the surface charge of a water droplet of a certain mass (41, 67–69).

## ACKNOWLEDGMENTS

This research was supported by grants R01-AI144022 and R01-AI118933 from the NIH to A.Z. We also acknowledge the Physical Biochemistry Instrumentation Facility and the IU Electron Microscopy Center, both which are supported by the Indiana CTSI.

## REFERENCES

- Graber-Stiehl I. 2018. The silent epidemic killing more people than HIV, malaria or TB. *Nature* 564:24–26. <https://doi.org/10.1038/d41586-018-07592-7>.
- Polaris Observatory Collaborators. 2018. Global prevalence, treatment, and prevention of hepatitis B virus infection in 2016: a modelling study. *Lancet Gastroenterol Hepatol* 3:383–403. [https://doi.org/10.1016/S2468-1253\(18\)30056-6](https://doi.org/10.1016/S2468-1253(18)30056-6).
- Viswanathan U, Mani N, Hu Z, Ban H, Du Y, Hu J, Chang J, Guo JT. 2020. Targeting the multifunctional HBV core protein as a potential cure for chronic hepatitis B. *Antiviral Res* 182:104917. <https://doi.org/10.1016/j.antiviral.2020.104917>.
- Venkatakrishnan B, Zlotnick A. 2016. The structural biology of hepatitis B virus: form and function. *Annu Rev Virol* 3:429–451. <https://doi.org/10.1146/annurev-virology-110615-042238>.
- Beck J, Nassal M. 2007. Hepatitis B virus replication. *World J Gastroenterol* 13:48–64. <https://doi.org/10.3748/wjg.v13.i1.48>.
- Prange R. 2012. Host factors involved in hepatitis B virus maturation, assembly, and egress. *Med Microbiol Immunol* 201:449–461. <https://doi.org/10.1007/s00430-012-0267-9>.
- Ceres P, Zlotnick A. 2002. Weak protein-protein interactions are sufficient to drive assembly of hepatitis B virus capsids. *Biochemistry* 41:11525–11531. <https://doi.org/10.1021/bi0261645>.
- Ning X, Nguyen D, Mentzer L, Adams C, Lee H, Ashley R, Hafenstein S, Hu J. 2011. Secretion of genome-free hepatitis B virus—single strand blocking model for virion morphogenesis of para-retrovirus. *PLoS Pathog* 7: e1002255. <https://doi.org/10.1371/journal.ppat.1002255>.
- Steven AC, Conway JF, Cheng N, Watts NR, Belnap DM, Harris A, Stahl SJ, Wingfield PT. 2005. Structure, assembly, and antigenicity of hepatitis B virus capsid proteins. *Adv Virus Res* 64:125–164. [https://doi.org/10.1016/S0065-3527\(05\)64005-5](https://doi.org/10.1016/S0065-3527(05)64005-5).
- Schlicksup CJ, Zlotnick A. 2020. Viral structural proteins as targets for antivirals. *Curr Opin Virol* 45:43–50. <https://doi.org/10.1016/j.coviro.2020.07.001>.
- Deres K, Schroder CH, Paessens A, Goldmann S, Hacker HJ, Weber O, Kramer T, Niewohner U, Pleiss U, Stoltefuss J, Graef E, Koletzki D, Masantschek RN, Reimann A, Jaeger R, Gross R, Beckermann B, Schlemmer KH, Haebich D, Rubsamen-Waigmann H. 2003. Inhibition of hepatitis B virus replication by drug-induced depletion of nucleocapsids. *Science* 299:893–896. <https://doi.org/10.1126/science.1077215>.
- Wang XY, Wei ZM, Wu GY, Wang JH, Zhang YJ, Li J, Zhang HH, Xie XW, Wang X, Wang ZH, Wei L, Wang Y, Chen HS. 2012. In vitro inhibition of HBV replication by a novel compound, GLS4, and its efficacy against adenofovir-dipivoxil-resistant HBV mutations. *Antivir Ther* 17:793–803. <https://doi.org/10.3851/IMP2152>.
- Bourne C, Lee S, Venkataiah B, Lee A, Korba B, Finn MG, Zlotnick A. 2008. Small-molecule effectors of hepatitis B virus capsid assembly give insight into virus life cycle. *J Virol* 82:10262–10270. <https://doi.org/10.1128/JVI.01360-08>.
- Stray SJ, Zlotnick A. 2006. BAY 41-4109 has multiple effects on hepatitis B virus capsid assembly. *J Mol Recognit* 19:542–548. <https://doi.org/10.1002/jmr.801>.
- Schlicksup CJ, Wang JC, Francis S, Venkatakrishnan B, Turner WW, VanNieuwenhze M, Zlotnick A. 2018. Hepatitis B virus core protein allosteric modulators can distort and disrupt intact capsids. *Elife* 7:e31473. <https://doi.org/10.7554/eLife.31473>.
- Berke JM, Dehertogh P, Vergauwen K, Mostmans W, Vandyck K, Rabaissou P, Pauwels F. 2020. Antiviral properties and mechanism of action studies of the hepatitis B virus capsid assembly modulator JNJ-56136379. *Antimicrob Agents Chemother* 64:e02439-19. <https://doi.org/10.1128/AAC.02439-19>.
- Berke JM, Dehertogh P, Vergauwen K, Van Damme E, Mostmans W, Vandyck K, Pauwels F. 2017. Capsid assembly modulators have a dual mechanism of action in primary human hepatocytes infected with hepatitis B virus. *Antimicrob Agents Chemother* 61:e00560-17. <https://doi.org/10.1128/AAC.00560-17>.
- Wang JC, Dhason MS, Zlotnick A. 2012. Structural organization of pregenomic RNA and the carboxy-terminal domain of the capsid protein of hepatitis B virus. *PLoS Pathog* 8:e1002919. <https://doi.org/10.1371/journal.ppat.1002919>.
- Birnbaum F, Nassal M. 1990. Hepatitis B virus nucleocapsid assembly: primary structure requirements in the core protein. *J Virol* 64:3319–3330. <https://doi.org/10.1128/JVI.64.7.3319-3330.1990>.
- Nassal M. 1992. The arginine-rich domain of the hepatitis B virus core protein is required for pregenome encapsidation and productive viral positive-strand DNA synthesis but not for virus assembly. *J Virol* 66:4107–4116. <https://doi.org/10.1128/JVI.66.7.4107-4116.1992>.
- Lewellyn EB, Loeb DD. 2011. The arginine clusters of the carboxy-terminal domain of the core protein of hepatitis B virus make pleiotropic contributions to genome replication. *J Virol* 85:1298–1309. <https://doi.org/10.1128/JVI.01957-10>.
- Kann M, Schmitz A, Rabe B. 2007. Intracellular transport of hepatitis B virus. *World J Gastroenterol* 13:39–47. <https://doi.org/10.3748/wjg.v13.i1.39>.

23. Li HC, Huang EY, Su PY, Wu SY, Yang CC, Lin YS, Chang WC, Shih C. 2010. Nuclear export and import of human hepatitis B virus capsid protein and particles. *PLoS Pathog* 6:e1001162. <https://doi.org/10.1371/journal.ppat.1001162>.
24. Yeh CT, Liaw YF, Ou JH. 1990. The arginine-rich domain of hepatitis B virus precore and core proteins contains a signal for nuclear transport. *J Virol* 64:6141–6147. <https://doi.org/10.1128/JVI.64.12.6141-6147.1990>.
25. Chen C, Wang JC-Y, Zlotnick A. 2011. A kinase chaperones hepatitis B virus capsid assembly and captures capsid dynamics in vitro. *PLoS Pathog* 7:e1002388. <https://doi.org/10.1371/journal.ppat.1002388>.
26. Chen C, Wang JC, Pierson EE, Keifer DZ, Delaleau M, Gallucci L, Cazenave C, Kann M, Jarrold MF, Zlotnick A. 2016. Importin beta can bind hepatitis B virus core protein and empty core-like particles and induce structural changes. *PLoS Pathog* 12:e1005802. <https://doi.org/10.1371/journal.ppat.1005802>.
27. Kann M, Sodeik B, Vlachou A, Gerlich WH, Helenius A. 1999. Phosphorylation-dependent binding of hepatitis B virus core particles to the nuclear pore complex. *J Cell Biol* 145:45–55. <https://doi.org/10.1083/jcb.145.1.45>.
28. Selzer L, Kant R, Wang JC, Bothner B, Zlotnick A. 2015. Hepatitis B virus core protein phosphorylation sites affect capsid stability and transient exposure of the C-terminal domain. *J Biol Chem* 290:28584–28593. <https://doi.org/10.1074/jbc.M115.678441>.
29. Zhao Q, Hu Z, Cheng J, Wu S, Luo Y, Chang J, Hu J, Guo JT. 2018. Hepatitis B virus core protein dephosphorylation occurs during pregenomic RNA encapsidation. *J Virol* doi:10.1128/JVI.02139–17. <https://doi.org/10.1128/JVI.02139-17>.
30. Heger-Stevic J, Zimmermann P, Lecoq L, Bottcher B, Nassal M. 2018. Hepatitis B virus core protein phosphorylation: identification of the SRPK1 target sites and impact of their occupancy on RNA binding and capsid structure. *PLoS Pathog* 14:e1007488. <https://doi.org/10.1371/journal.ppat.1007488>.
31. Rabe B, Vlachou A, Pante N, Helenius A, Kann M. 2003. Nuclear import of hepatitis B virus capsids and release of the viral genome. *Proc Natl Acad Sci U S A* 100:9849–9854. <https://doi.org/10.1073/pnas.1730940100>.
32. Schmitz A, Schwarz A, Foss M, Zhou L, Rabe B, Hoellenriegel J, Stoeber M, Pante N, Kann M. 2010. Nucleoporin 153 arrests the nuclear import of hepatitis B virus capsids in the nuclear basket. *PLoS Pathog* 6:e1000741. <https://doi.org/10.1371/journal.ppat.1000741>.
33. Rabe B, Delaleau M, Bischof A, Foss M, Sominskaya I, Pumpens P, Cazenave C, Castroviejo M, Kann M. 2009. Nuclear entry of hepatitis B virus capsids involves disintegration to protein dimers followed by nuclear reassociation to capsids. *PLoS Pathog* 5:e1000563. <https://doi.org/10.1371/journal.ppat.1000563>.
34. Kann M, Thomssen R, Kochel HG, Gerlich WH. 1993. Characterization of the endogenous protein kinase activity of the hepatitis B virus. *Arch Virol Suppl* 8:53–62. [https://doi.org/10.1007/978-3-7091-9312-9\\_6](https://doi.org/10.1007/978-3-7091-9312-9_6).
35. Osseman Q, Kann M. 2017. Intracytoplasmic transport of hepatitis B virus capsids. *Methods Mol Biol* 1540:37–51. [https://doi.org/10.1007/978-1-4939-6700-1\\_4](https://doi.org/10.1007/978-1-4939-6700-1_4).
36. Cingolani G, Petosa C, Weis K, Muller CW. 1999. Structure of importin-beta bound to the IBB domain of importin-alpha. *Nature* 399:221–229. <https://doi.org/10.1038/20367>.
37. Hilmer JK, Zlotnick A, Bothner B. 2008. Conformational equilibria and rates of localized motion within hepatitis B virus capsids. *J Mol Biol* 375:581–594. <https://doi.org/10.1016/j.jmb.2007.10.044>.
38. Porterfield JZ, Dhasan MS, Loeb DD, Nassal M, Stray SJ, Zlotnick A. 2010. Full-length hepatitis B virus core protein packages viral and heterologous RNA with similarly high levels of cooperativity. *J Virol* 84:7174–7184. <https://doi.org/10.1128/JVI.00586-10>.
39. Chua PK, Tang FM, Huang JY, Suen CS, Shih C. 2010. Testing the balanced electrostatic interaction hypothesis of hepatitis B virus DNA synthesis by using an in vivo charge rebalance approach. *J Virol* 84:2340–2351. <https://doi.org/10.1128/JVI.01666-09>.
40. Schlicksup CJ, Laughlin P, Dunkelbarger S, Wang JC, Zlotnick A. 2020. Local stabilization of subunit-subunit contacts causes global destabilization of hepatitis B virus capsids. *ACS Chem Biol* 15:1708–1717. <https://doi.org/10.1021/acscchembio.0c00320>.
41. Rayleigh L. 1882. XX. On the equilibrium of liquid conducting masses charged with electricity. *Philos Mag* 14:184–186. <https://doi.org/10.1080/14786448208628425>.
42. Lutomski CA, Gordon SM, Remaley AT, Jarrold MF. 2018. Resolution of lipoprotein subclasses by charge detection mass spectrometry. *Anal Chem* 90:6353–6356. <https://doi.org/10.1021/acs.analchem.8b01127>.
43. Cui X, Ludgate L, Ning X, Hu J. 2013. Maturation-associated destabilization of hepatitis B virus nucleocapsid. *J Virol* 87:11494–11503. <https://doi.org/10.1128/JVI.01912-13>.
44. Dhasan MS, Wang JC, Hagan MF, Zlotnick A. 2012. Differential assembly of hepatitis B virus core protein on single- and double-stranded nucleic acid suggest the dsDNA-filled core is spring-loaded. *Virology* 430:20–29. <https://doi.org/10.1016/j.virol.2012.04.012>.
45. Stray SJ, Bourne CR, Punna S, Lewis WG, Finn MG, Zlotnick A. 2005. A heteroaryldihydropyrimidine activates and can misdirect hepatitis B virus capsid assembly. *Proc Natl Acad Sci U S A* 102:8138–8143. <https://doi.org/10.1073/pnas.0409732102>.
46. Venkatakrishnan B, Katen SP, Francis S, Chirapu S, Finn MG, Zlotnick A. 2016. Hepatitis B virus capsids have diverse structural responses to small-molecule ligands bound to the heteroaryldihydropyrimidine pocket. *J Virol* 90:3994–4004. <https://doi.org/10.1128/JVI.03058-15>.
47. Rudnick J, Bruinsma R. 2005. Icosahedral packing of RNA viral genomes. *Phys Rev Lett* 94:e038101. <https://doi.org/10.1103/PhysRevLett.94.038101>.
48. Nair S, Zlotnick A. 2018. Asymmetric modification of hepatitis B virus (HBV) genomes by an endogenous cytidine deaminase inside HBV cores informs a model of reverse transcription. *J Virol* 92:e02190-17. <https://doi.org/10.1128/JVI.02190-17>.
49. Dykeman EC, Grayson NE, Toropova K, Ranson NA, Stockley PG, Twarock R. 2011. Simple rules for efficient assembly predict the layout of a packaged viral RNA. *J Mol Biol* 408:399–407. <https://doi.org/10.1016/j.jmb.2011.02.039>.
50. Yau ST, Thomas BR, Galkin O, Gliko O, Vekilov PG. 2001. Molecular mechanisms of microheterogeneity-induced defect formation in ferritin crystallization. *Proteins* 43:343–352. <https://doi.org/10.1002/prot.1047>.
51. Reference deleted.
52. Katen SP, Tan Z, Chirapu SR, Finn MG, Zlotnick A. 2013. Assembly-directed antivirals differentially bind quasiequivalent pockets to modify hepatitis B virus capsid tertiary and quaternary structure. *Structure* 21:1406–1416. <https://doi.org/10.1016/j.str.2013.06.013>.
53. Seeger C, Mason WS. 2015. Molecular biology of hepatitis B virus infection. *Virology* 479-480:672–686. <https://doi.org/10.1016/j.virol.2015.02.031>.
54. Sun L, Wu J, Du F, Chen X, Chen ZJ. 2013. Cyclic GMP-AMP synthase is a cytosolic DNA sensor that activates the type I interferon pathway. *Science* 339:786–791. <https://doi.org/10.1126/science.1232458>.
55. Guo F, Zhao Q, Sheraz M, Cheng J, Qi Y, Su Q, Cuconati A, Wei L, Du Y, Li W, Chang J, Guo JT. 2017. HBV core protein allosteric modulators differentially alter cccDNA biosynthesis from de novo infection and intracellular amplification pathways. *PLoS Pathog* 13:e1006658. <https://doi.org/10.1371/journal.ppat.1006658>.
56. Chopra A, Willmore WG, Biggar KK. 2019. Protein quantification and visualization using ultraviolet-dependent labeling with 2,2,2-trichloroethanol. *Sci Rep* 9:13923. <https://doi.org/10.1038/s41598-019-50385-9>.
57. Schindelin J, Arganda-Carreras I, Frise E, Kaynig V, Longair M, Pietzsch T, Preibisch S, Rueden C, Saalfeld S, Schmid B, Tinevez JY, White DJ, Hartenstein V, Eliceiri K, Tomancak P, Cardona A. 2012. Fiji: an open-source platform for biological-image analysis. *Nat Methods* 9:676–682. <https://doi.org/10.1038/nmeth.2019>.
58. Burns EE, Keith BK, Refai MY, Bothner B, Dyer WE. 2017. Proteomic and biochemical assays of glutathione-related proteins in susceptible and multiple herbicide resistant *Avena fatua* L. *Pestic Biochem Physiol* 140:69–78. <https://doi.org/10.1016/j.pestbp.2017.06.007>.
59. Ledbetter RN, Garcia Costas AM, Lubner CE, Mulder DW, Tokmina-Lukaszewska M, Artz JH, Patterson A, Magnuson TS, Jay ZJ, Duan HD, Miller J, Plunkett MH, Hoben JP, Barney BM, Carlson RP, Miller AF, Bothner B, King PW, Peters JW, Seefeldt LC. 2017. The electron bifurcating FixABCX protein complex from *Azotobacter vinelandii*: generation of low-potential reducing equivalents for nitrogenase catalysis. *Biochemistry* 56:4177–4190. <https://doi.org/10.1021/acs.biochem.7b00389>.
60. Vaudel M, Burkhart JM, Zahedi RP, Oveland E, Berven FS, Sickmann A, Martens L, Barsnes H. 2015. PeptideShaker enables reanalysis of MS-derived proteomics data sets. *Nat Biotechnol* 33:22–24. <https://doi.org/10.1038/nbt.3109>.
61. Barsnes H, Vaudel M. 2018. SearchGUI: a highly adaptable common interface for proteomics search and de novo engines. *J Proteome Res* 17:2552–2555. <https://doi.org/10.1021/acs.jproteome.8b00175>.
62. Kremer JR, Mastrorade DN, McIntosh JR. 1996. Computer visualization of three-dimensional image data using IMOD. *J Struct Biol* 116:71–76. <https://doi.org/10.1006/jsbi.1996.0013>.

63. Frangakis AS, Hegerl R. 2001. Noise reduction in electron tomographic reconstructions using nonlinear anisotropic diffusion. *J Struct Biol* 135: 239–250. <https://doi.org/10.1006/jsbi.2001.4406>.
64. Contino NC, Jarrold MF. 2013. Charge detection mass spectrometry for single ions with a limit of detection of 30 charges. *Int J Mass Spectrom* 345–347:153–159. <https://doi.org/10.1016/j.ijms.2012.07.010>.
65. Draper BE, Anthony SN, Jarrold MF. 2018. The FUNPET—a new hybrid ion funnel-ion carpet atmospheric pressure interface for the simultaneous transmission of a broad mass range. *J Am Soc Mass Spectrom* 29:2160–2172. <https://doi.org/10.1007/s13361-018-2038-3>.
66. Draper BE, Jarrold MF. 2019. Real-time analysis and signal optimization for charge detection mass spectrometry. *J Am Soc Mass Spectrom* 30: 898–904. <https://doi.org/10.1007/s13361-019-02172-z>.
67. de la Mora JF. 2000. Electrospray ionization of large multiply charged species proceeds via Dole's charge residue mechanism. *Anal Chim Acta* 406: 93–104. [https://doi.org/10.1016/S0003-2670\(99\)00601-7](https://doi.org/10.1016/S0003-2670(99)00601-7).
68. Konermann L, Ahadi E, Rodriguez AD, Vahidi S. 2013. Unraveling the mechanism of electrospray ionization. *Anal Chem* 85:2–9. <https://doi.org/10.1021/ac302789c>.
69. Keifer D, Motwani T, Teschke CM, Jarrold MF. 2016. Acquiring structural information on virus particles via charge detection mass spectrometry. *J Am Soc Mass Spectrom* 27:1028–1036. <https://doi.org/10.1007/s13361-016-1362-8>.